RSC Advances

REVIEW

View Article Online
View Journal | View Issue

Cite this: *RSC Adv.*, 2025, **15**, 28204

Recent advances in TiO_2 modification for improvement in photocatalytic purification of indoor VOCs

Lian Yu, *[a] Yajing Duan,[a] Dabin Wang,[b] Zhen Liang,[c] Cunzhen Liang[a] and Yafei Wang[a]

Received 26th April 2025
Accepted 22nd July 2025

DOI: 10.1039/d5ra02935j

rsc.li/rsc-advances

TiO_2-based photocatalytic oxidation technology has been widely used for the purification of indoor VOCs. However, the fast recombination rates of photoexcited charge carriers and wide energy band gaps have limited the practical application of TiO_2-based photocatalysts. Therefore, developing highly efficient catalysts is crucial for efficiently separating charge carriers and hindering their recombination, fully utilizing visible light. There are four main methods to improve TiO_2 photocatalytic activity: increasing e^-–h^+ separation rates and decreasing e^-–h^+ recombination rates, increasing visible light photocatalytic activity, increasing surface-active sites, and increasing physicochemical stability. Metal and non-metal doping, coupling of different semiconductors, surface and interface design, and TiO_2 immobilization are usually used to enhance the photocatalytic activity of TiO_2. This review aims to improve photocatalytic purification efficiency for indoor VOCs, and may provide new insights and guidance for the design of novel photocatalysts based on the intrinsic characteristics of VOCs, such as high volatility, low molecular weight, low polarity, high hydrophobicity, strong chemical activity and high toxicity.

1. Introduction

Nowadays, most people spend more than 80% of their time in indoors, such as in the office, home, shopping centre or car, so indoor air quality has attracted extensive attention. Many kinds of volatile organic compounds (VOCs) have been detected in indoor air, including aliphatic hydrocarbons, aromatic hydrocarbons, chlorinated hydrocarbons, ketones, and aldehydes.[1] The main sources of VOCs can be classified into three kinds: endogenous sources, reaction products from the indoor environment, and outdoor sources. Endogenous sources consist mainly of permanent and occasional sources. Permanent sources include releases from building materials, adhesives, laminated materials, plywood, insulators, and paints.[2] The occasional sources can be attributed to human activities, such as the use of different disinfection products, cleaning, cooking and personal care. Smoking was an important source of indoor VOCs, and more than 78 kinds of compounds (such as polycyclic aromatic hydrocarbons, aromatics, carbonyls, and quinones) were detected in cigarette gases.[3] Human metabolism was regarded as an endogenous source of indoor VOCs: 199 kinds of VOCs have been identified in human breath, such as isoprene and acetone.[4] Apart from direct emission of VOCs from indoor sources, the products from gas-phase reactions indoors were also sources of indoor VOCs. Outdoor air pollutants were derived mainly from road traffic, industry, and the combustion of fossil fuels.[5] In addition, natural sources can also release VOCs (such as biological VOCs, from metabolic reactions of vegetation) to the outdoor atmosphere.[6]

The concentration of indoor VOCs depended strongly on the existence of emission sources and conditions of ventilation. The concentrations of indoor single VOCs were generally below 15 ppb, and most were below 1.5 ppb.[7] Most VOCs were toxic, and some were carcinogenic, teratogenic or mutagenic. Long-term exposure to VOCs can cause chronic diseases, such as inflammation of the nasal passages and throat, dizziness, and headaches, and they can even cause cancer.[8] Exposure to low concentrations can cause damage to the prior respiratory system,[9] while exposure to high concentrations can depress the central nervous system.[10] Benzene and toluene can cause myelodysplastic syndrome.[9] Formaldehyde can cause immune dysfunction and intellectual decline, and it may even cause colon cancer, nasopharyngeal cancer, leukemia and brain tumors.[11] Currently, millions of people are suffering from the effects of poor indoor air quality; VOCs are the main source of indoor air pollution, and billions of dollars are lost worldwide each year.[12] It is essential to find an efficient and feasible method to remove VOCs from the indoor environment. In general, three kinds of methods were proposed to remove VOCs

[a]*Department of Environmental Engineering, Beijing Institute of Petrochemical Technology, Beijing 102617, PR China. E-mail: yulian@bipt.edu.cn*
[b]*Laboratory of Quality & Safety Risk Assessment for Tobacco, Ministry of Agriculture, Tobacco Research Institute of Chinese Academy of Agricultural Sciences, Qingdao, 266101, PR China*
[c]*College of Fisheries, Southwest University, Chongqing, 402460, PR China*

from indoor air: source control, ventilation, and air cleaning.[13] Source control was usually uncontrollable, and increased ventilation may transport other outdoor pollutants to the indoor environment. Therefore, air cleaning was considered the most feasible method to remove VOCs from indoor air.

Many efficient and feasible air cleaning technologies for indoor VOC removal have been developed, such as adsorption,[14] membrane separation,[15] microbial routes,[16] catalytic combustion,[17] thermal catalysis,[18] non-thermal plasmas[19] and photocatalysis.[20] However, all these methods showed significant limitations for practical application, and it was difficult for these methods to achieve efficient and safe purification for indoor VOCs. Adsorption consumed low energy, but the adsorbents required frequent regeneration, and the adsorbed VOCs may be released to the environment again during adsorbent regeneration.[21] The cost of membrane separation was high, and there existed the problem of membrane fouling. The microbial route required large-scale facilities to carry out the process. Catalytic combustion, thermal catalysis, and non-thermal plasmas were effective, but they consumed a lot of energy.[22] Photocatalysis usually occurred at room temperature and atmospheric pressure, so it was theoretically, technically and economically competitive with other techniques.[23] In the middle of the 1990s, photocatalysis was first used for air purification in Japan.[24] The photocatalysts commonly used in photocatalytic oxidation (PCO) were metal oxides or sulfides, such as TiO_2, ZnO, SnO_2, ZrO_2, CeO_2, WO_3, Al_2O_3, Fe_2O_3, ZnS and CdS.[25]

Due to its high photocatalytic activity, non-selectivity in oxidation reactions, easy synthesis and immobilization on support materials, high stability, colorlessness, non-toxicity, as well as cheapness, TiO_2 was most commonly used for indoor air purification.[26] TiO_2-based photocatalytic technology solved three main problems in indoor VOC purification: insufficient adsorption, incomplete oxidation, and high costs for treatment. However, there were some drawbacks for TiO_2, such as a high charge carrier recombination rate and inefficient utilization of visible light, low adsorption capacity for VOCs, the production of hazardous intermediate products, and deactivation of photocatalysts, and many strategies have been used to overcome the defects of TiO_2: for example, ion doping, the formation of oxygen vacancies, the construction of heterojunctions and homojunctions, surface halogenation, facet engineering, specific surface area and pore structure modulation.

Because of the inefficient utilization of visible light, photogenerated electrons from the valence band of TiO_2 can only be induced under ultraviolet (UV) light irradiation, and many researchers have tried to develop novel TiO_2-based catalysts with low band gaps, using methods such as metal and non-metal doping, and coupling with different semiconductors.[27] Although they can improve the absorption of visible light, the dopants may act as recombination centers for photoinduced electrons and holes.[28] Oxygen vacancies and active facets were beneficial to activate VOC molecules, and surface halogenation adjusted the performance of the TiO_2 surface and promoted VOC adsorption.[29] The larger pore structure was favourable for mass transfer, and the larger specific surface area could provide more active sites.[30] The crystallinity, crystal size, porosity, surface area, surface morphology, energy band structure and adsorption performance were also adjusted to enhance the photocatalytic activity of TiO_2.[31] The photocatalytic purification of indoor VOCs involved the following main steps: diffusion, external and internal mass transfer, adsorption of VOCs on the surface of the photocatalysts, VOC degradation, desorption of products, and transfer of products to the airflow. Methods for TiO_2 modification which can enhance the efficiency of the above steps can also improve photocatalytic purification performance for indoor VOCs.

In the past two decades, TiO_2-based photocatalytic oxidation for the removal of indoor VOCs has attracted extensive interest, and some reviews have been published.[8,22,26,27,31–33] As far as we know, there have only been a few reviews which comprehensively and thoroughly summarized methods for improving the photocatalytic purification performance of indoor VOCs from the perspective of TiO_2 modification.[3,27,32] The methods of TiO_2 modification to improve removal efficiency for indoor VOCs focused mainly on an increase in e^-–h^+ separation rates and a decrease in e^-–h^+ recombination rates, an increase in visible light photocatalytic activity, an increase in surface-active sites, and an increase of physicochemical stability. In this review, five kinds of modification methods are summarized for improving indoor VOCs photocatalytic degradation based on promoting charge carrier separation and visible light absorption for TiO_2-based photocatalysts: (1) metal doping and surface loading; (2) non-metal doping; (3) metal and non-metal co-doping; (4) surface and interface design; (5) immobilization of photocatalysts. This review will aid a deep understanding of recent advances in the application of TiO_2-based photocatalytic technology for the purification of indoor VOCs at ambient temperature, especially for aromatic hydrocarbons and aldehydes. It will also provide new insights and guidance for the design of efficient photocatalysts based on the intrinsic characteristics of pollutants.

2. Metal doping and surface deposition

Both metal and non-metal doping can induce new doping levels inside the TiO_2 band gap; they can change its electronic structure, thus reducing its high band-gap energy (Fig. 1). The photocatalytic performance depended strongly on the chemical nature and concentration of dopants, catalyst preparation, and thermal treatment method.[27] Under visible light irradiation, photoinduced electrons from the TiO_2 valence band can be transferred to the doping levels inside the TiO_2 band gap.[35] Metal doping can introduce additional states near the TiO_2 conduction band by substituting metal ions of Ti^{4+}; electrons are transferred from the TiO_2 conduction band to the doping states; at the same time, they can be also excited from the TiO_2 valence band to the doping states by photons whose energy is less than 3.2 eV, which can lower the band gap of TiO_2.[36] Metal ion doping influences TiO_2 photocatalysis according to the following principles:[37] (1) an improvement in the separation of

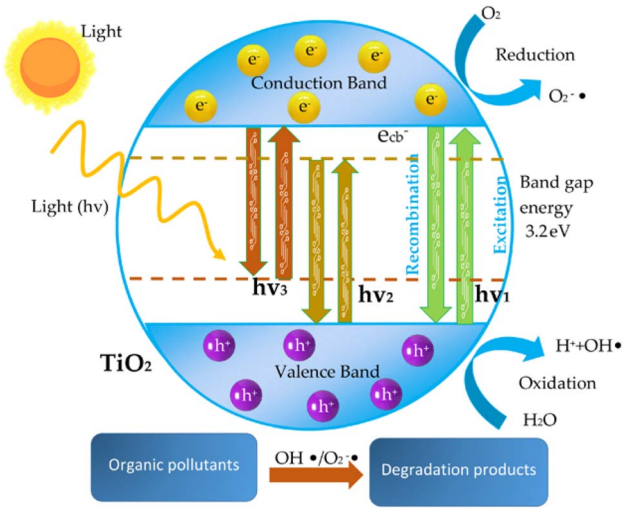

Fig. 1 Mechanism of TiO_2 photocatalysis—hv_1: pure TiO_2; hv_2: metal-doped TiO_2, and hv_3: non-metal-doped TiO_2.[34] Reprinted with permission from ref. 34 Copyright 2023, MDPI.

electrons and holes by selective trapping; (2) extension of optical absorption to the visible light range; (3) a decrease in the carrier lifespan due to acting as recombination centers.

Noble metals (such as gold and silver) depend mainly on surface electron trap and plasmon resonance effects; rare earth elements (such as cerium and lanthanum) with 4f orbitals can introduce impurity levels into the band gap of TiO_2 and also hinder recombination of electrons and holes; and transition metals (such as iron and chromium) can change the band gap by forming impurity levels. Precious metals are costly, but the catalysts showed strong photocatalytic activity; rare earth elements showed selectivity for specific pollutants; transition metals are cheap, but they may introduce recombination centers. The visible light photocatalytic efficiency of metal-doped TiO_2 not only rested with a red shift of the absorption spectra but also depended on the generated and recombined rates of electrons and holes. Even though metal doping can extend optical absorption to the visible light range, the photocatalytic activity decreased significantly in the UV region.[38] Commonly used metal dopants, such as noble metals, rare earth metals, transition metals, and their properties are discussed in following sections.

2.1. Noble metal deposition

Unlike most metals, noble metals showed high stability in corrosion and oxidation conditions in humid air. There existed localized surface plasmon resonance (LSPR) for noble metals, which enabled efficient visible light harvesting, plasmon resonance energy transfer (PRET), the generation of hot electrons and holes, scattering, and the photothermal heating effect (Fig. 2).[39] Deposition of noble metals onto TiO_2 was favorable for efficient light-harvesting and absorption, and it could effectively hinder charge carrier recombination due to the Schottky barrier generated at the interface of the metal and TiO_2 junction.[40] LSPR excitation can generate LSPR-excited charge carriers under visible light, then charge carriers are transferred at the metal–semiconductor interface, and energetic hot electrons are directly injected into the CB of the adjacent semiconductor (Fig. 2(a)). LSPR excitation can lead to the formation of intense electric fields near the surface of noble metals, and the electric fields can improve light absorption by the nearby semiconductor (Fig. 2(b)). After energy absorption from light by noble metals, resonant energy can be transferred to the adjacent semiconductor through dipole–dipole coupling, leading to the production of charge carriers near and below the semiconductor band edge (Fig. 2(c)).[40]

Noble metals, like Pd,[42] Pt,[40] Au,[43] Ag,[44] Ru,[45] and Ir,[46] can expand the optical absorption of TiO_2 to the visible light range. Au and Ag were the most widely used for improving visible light photocatalytic degradation efficiency of TiO_2 for VOCs, such as formaldehyde, methanol, ethylene, and many other VOCs.[39] The SPR effect promoted the photocatalytic activity of plasmonic Au/TiO_2; hot electrons (SPR state) from Au directly injected into the TiO_2 conduction band can reduce O_2 (an electron acceptor) to form $^{\bullet}O_2^-$ at the interface of TiO_2 and Au; at the same time, $Au^{\delta+}$ cations (from SPR) can migrate to the interface of TiO_2 and Au to facilitate formaldehyde oxidation decomposition (particularly for formate and carbonate) and form $^{\bullet}OH$ *via* H_2O oxidation.

Au/TiO_2 was used for formaldehyde oxidation, under visible light irradiation, and the photocatalytic degradation efficiency of formaldehyde was about 83.3% over 1.07% Au/TiO_2, while formaldehyde conversion decreased to 22.3% over 0.2% Au/TiO_2.[43] In wet air (44% RH), 83.3% of formaldehyde was completely removed under visible light, while in dry air, the

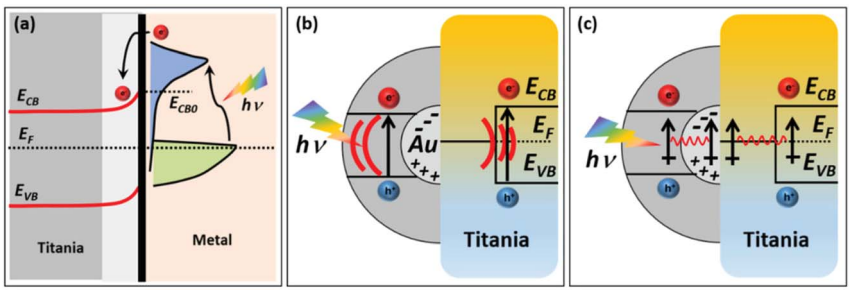

Fig. 2 Schematic of the energy transfer processes at the metal–semiconductor interface by LSPR excitation: (a) hot-electron generation and transfer to the semiconductor CB, (b) enhancement of absorption near-field EM, and (c) energy transfer by plasmon resonance.[39] Reprinted with permission from ref. 39 Copyright 2022, John Wiley and Sons.

catalyst was inactive, so moisture is indispensable for the decomposition of carbonate and could promote the oxidation of dioxymethylene to formate; visible light could accelerate formate oxidation to carbonate and its further decomposition, which were the rate-determining steps.[43] Ag species were deposited onto titania nanotubes (TNTs), and metallic Ag could be easily converted to Ag_2O; surface oxygen and Ag_2O species were responsible for the production of ROSs; metallic Ag could generate hot electrons under visible light irradiation; toluene (30 ppm) could be effectively decomposed (~83.3%) and mineralized (~70.7%) in 3 h under UV-visible light irradiation; an appropriate Ag/Ag_2O ratio on TNT film was crucial for improving photocatalytic performance.[44]

Deposition of noble metals can also relieve the deactivation of photocatalysts: the deposition of Pd could effectively remove the inherent –OH groups on the surface of TiO_2, which notably promoted O_2 activation, thus accelerating the degradation of toluene and xylenes and producing aromatic aldehydes and ring-opening products, avoiding the formation of methylphenolics, which could lead to the deactivation of catalysts.[42] Pd/TiO_2 (1 wt%) showed excellent performance for the photocatalytic degradation of toluene under UV light, and the production of toxic methylphenols was suppressed compared with pure TiO_2.[42] Pd/TiO_2 (1 wt%) was used for the photocatalytic oxidation of benzene in air; metallic (Pd^0) and oxidized (PdO_x) palladium could form on the TiO_2 surface; in addition to increase the photocatalytic activity for oxidation of benzene, Pd nanoparticles could also suppress the production of CO and other intermediates during the photocatalytic reaction process and increase air purification efficiency.[47] The photocatalytic oxidation of toluene over Pd/TiO_2–N mainly followed the process: toluene → benzyl alcohol → benzaldehyde → benzoic acid → maleate, short-chain carboxylate and aldehyde/ketone (acetone) → CO_2 and H_2O, as shown in Fig. 3.[41]

2.2. Rare earth metals

Rare earth metals contain 17 kinds of chemical elements, Sc, Y and 15 lanthanides, where these elements possess incomplete 4f orbitals and empty 5d orbitals. Doping TiO_2 with rare earth cations can increase light absorption, modifying the phase structure, morphology and surface area of the catalysts. Additionally, doping with rare earth ions can hinder the phase change from anatase to rutile.[49] Recently, doping with lanthanide group metals has attracted more and more attention. For Nd-doped TiO_2, the substitutional incorporation of Nd^{3+} distorted the TiO_2 lattice because of the significantly larger Nd^{3+} ionic radius (0.983 Å) than that of Ti^{4+} ion (0.605 Å), and Ti^{4+} ions replacing Nd^{3+} in the neodymium oxides lattice produced a Ti–O–Nd bond.[50] As a result, the lattice crystallite size of TiO_2 decreased, and some defects formed in the TiO_2 crystallite. An optimum content of dopant (1 mol%) was crucial to improve the photocatalytic activity of Nd-doped TiO_2. The interaction of Nd ions and Ti^{4+} can generate Ti^{3+} ions, inhibiting the recombination of photoinduced electrons and holes.[50]

It was indicated that doping with rare earth metal ions could improve the adsorption capacity of TiO_2 for organic pollutants (Fig. 4),[51] and the incorporation of lanthanide ions (like La^{3+}, Nd^{3+}, Eu^{3+}, Pr^{3+}, and Sm^{3+}) into the TiO_2 lattice could facilitate the chemical and physical adsorption of organic pollutants on the surface of the catalysts, thus improving TiO_2 photocatalytic activity.[52] TiO_2 modified with Er single atoms and Er^{3+} ions showed high adsorption capacity and strong ability to generate ROSs. The catalysts showed excellent performance for the photocatalytic degradation of *o*-xylene and acetaldehyde, and were more inclined to produce intermediates and simplify degradation reactions instead of the generation of CO_2 when they were used for the photocatalytic degradation of an *o*-xylene–acetaldehyde mixture.[53]

2.3. Transition metals

The most commonly used transition metals were Mn,[35] Fe,[55] Cu,[56] V,[57] Cr,[58] Co[59] and Ni.[60] Doping with transition metals can

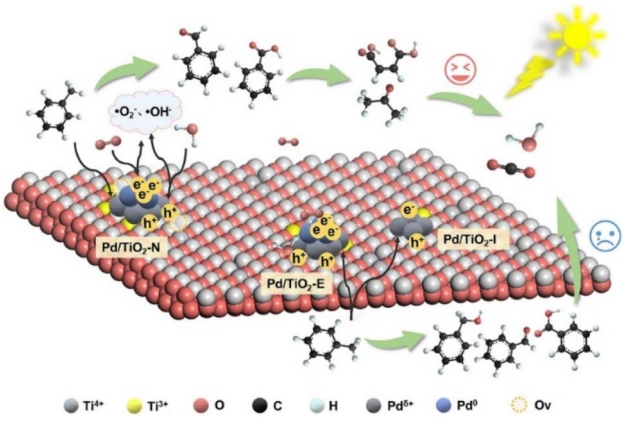

Fig. 3 The reaction pathway of toluene photocatalytic oxidation over Pd/TiO_2 catalysts.[41] Reprinted with permission from ref. 41 Copyright 2023, Elsevier.

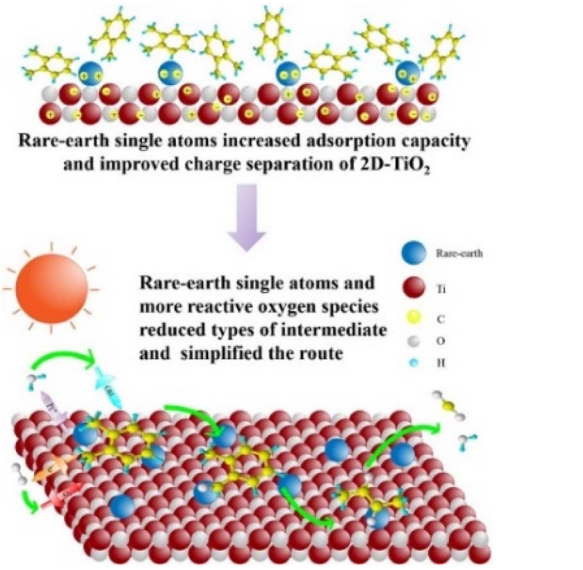

Fig. 4 Schematic of and charge separation of TiO_2 modified with rare-earth single atoms and *o*-xylene adsorption and photocatalytic degradation process over modified TiO_2.[48] Reprinted with permission from ref. 48 Copyright 2022, Elsevier.

reduce the energy band gap, and hinder recombination of electrons and holes.[35] For transition metals, the type and amount were two key parameters affecting the photocatalytic reaction. When the amount of metal dopants was kept at the optimum level, the dopants could serve as a bridge for charge carriers, which promoted the separation of electrons and holes, but, when the amount of dopants was above the optimum level, they might have distorted the crystallinity of the catalysts and become recombination centers for photogenerated charge carriers.[55] After doping beyond the optimum amount of transition metals (Cu, Ni, Mn, Co, and Fe), the catalyst surface area decreased, because they might have blocked TiO_2 pores or induced the agglomeration of particles.

M-modified TiO_2 (where M = Fe, Cu, Co, Zn and Ni) showed notably higher photocatalytic activity than pure TiO_2 under both UV and visible light irradiation; Cu/TiO_2 showed the best performance, where Cu species were uniformly dispersed on the surface of TiO_2 and existed as both oxidized Cu^{2+} and reduced Cu^0/Cu^+, where the ratio of Cu^0/Cu^+ to Cu^{2+} decreased during the photocatalysis process, due to the transfer of photogenerated electrons and holes under UV or visible light.[61] CuO_x clusters were loaded onto the surface of TiO_2; Cu dopants could substitute Ti^{4+} ions; and some defects were produced in the TiO_2 lattice *via* the formation of Cu–O–Ti bonds; Cu^{2+} and Cu^+ in CuO_x clusters/TiO_2 showed high redox reversibility, which greatly promoted the separation of holes and electrons, thus enhancing the photocatalytic oxidation efficiency of HCHO under visible light; the introduction of H_2O greatly promoted HCHO oxidation, and $^{\bullet}OH$ played a critical role in formate decomposition, rather than $^{\bullet}O_2^-$.[56]

The position of the TiO_2 VB and CB edges can be adjusted by Fe and Cu doping (Fig. 6).[54] After Cu^+ and Fe^{3+}/Fe^{2+} doping, the wavelength at the tangential point of the extrapolated slope increased from 410 nm to 780 nm and 500 nm, which can be attributed to the absorption of Cu_2O and iron oxides; for Cu^+ and Fe^{3+}/Fe^{2+} co-doping, these peaks were slightly reduced and blue-shifted (Fig. 5(a)). The band gaps of TiO_2, $10CuTiO_2$, $10FeTiO_2$, and $5Cu5FeTiO_2$ were 2.91, 2.89, 2.38, and 2.48 eV,

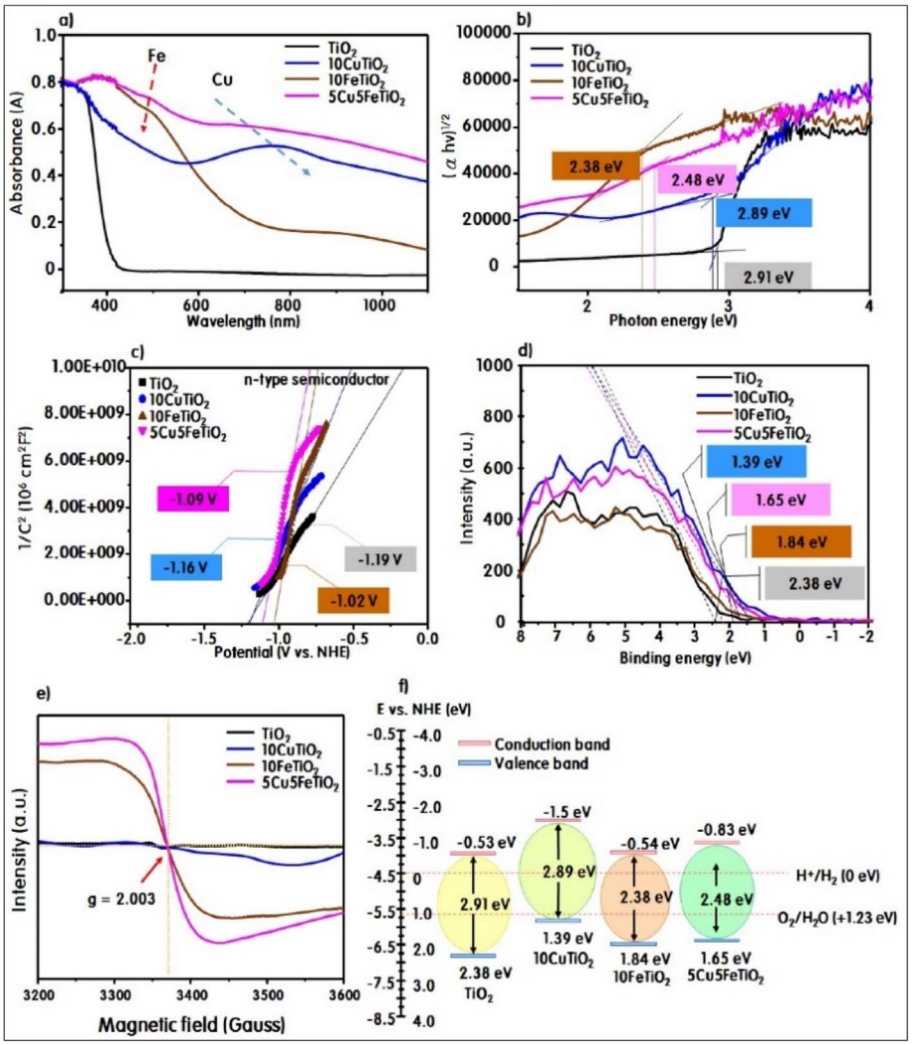

Fig. 5 DRS UV-visible absorption spectra (a), Tauc plots (b), Mott–Schottky plots (c), XPS-VB curves (d), EPR curves (e), energy diagrams of the catalyst (f) based on VBM, CBM, and band gaps.[54] Reprinted with permission from ref. 54 Copyright 2024, Elsevier.

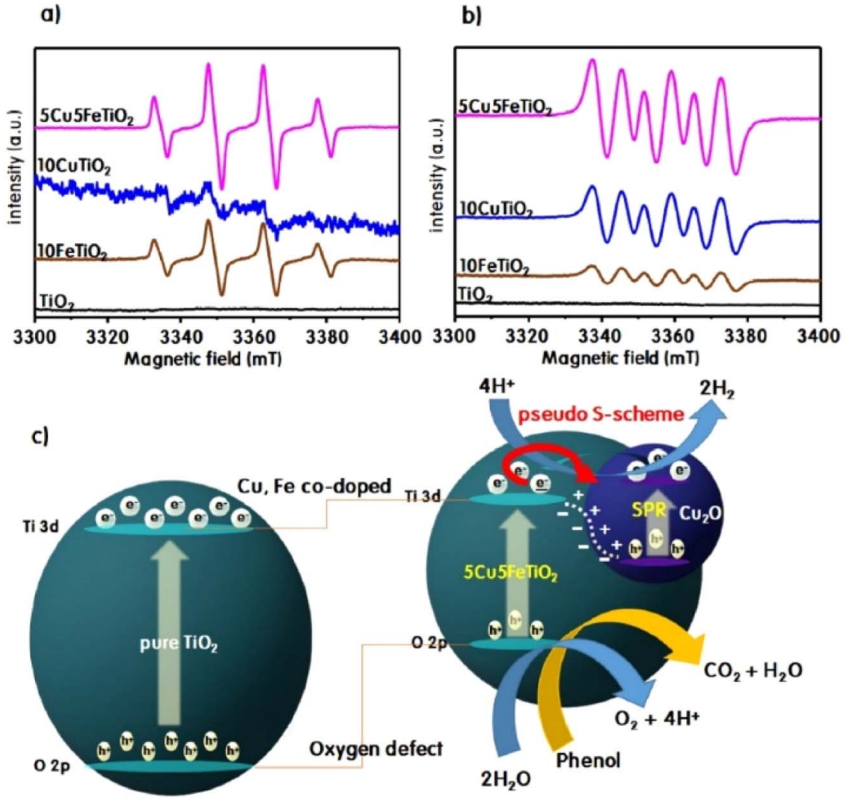

Fig. 6 DMPO-$^{\bullet}$OH (a) and $^{\bullet}O_2^-$ (b) radical ESR trapping signals under light irradiation of each sample, and charge transfer and reaction mechanism over 5Cu5FeTiO$_2$ (c).[54] Reprinted with permission from ref. 54 Copyright 2024, Elsevier.

respectively (Fig. 5(b)).[54] The Mott–Schottky curves exhibited a positive slope; Cu-doped regions facilitated electron transfer; while Fe-doped regions enhanced hole transfer, which inhibited electron–hole recombination and promoted the formation of ROS (Fig. 5(c)). From XPS-VBM (valence band maximum) and EPR analysis (Fig. 5(d and e)), the co-doping of Cu^+ and Fe^{3+}/Fe^{2+} into the TiO$_2$ lattice promoted the formation of oxygen vacancies through interaction with the electronic structure, which further enhanced the catalytic performance.[54] Compared to pure TiO$_2$, the insertion of Cu^+ shifted the VBM energy level upward, while the insertion of Fe^{3+}/Fe^{2+} shifted the CBM (conduction band maximum) energy level downward (Fig. 5(f)), which resulted in a reduced band gap; as for Cu^+ and Fe^{3+}/Fe^{2+} co-doping, both VBM and CBM levels decreased, resulting in a significant reduction in the band gap.[54] 5Cu5FeTiO$_2$ showed much stronger signals for both DMPO-$^{\bullet}$OH and DMPO-$^{\bullet}O_2^-$, suggesting that phenol oxidation was efficient (Fig. 6(a and b)), indicating a synergistic effect between copper and iron.

3. Non-metal doping of TiO$_2$

Anions can substitute oxygen in the TiO$_2$ lattice; the TiO$_2$ band gap can be narrowed by doping with non-metal (anions) rather than cations; and non-metal dopants form new states close to the valence band, which lowers the TiO$_2$ band gap.[64] Among non-metal dopants, N,[65] C,[66] S,[67] B,[68] and F,[69] showed promising results for improving TiO$_2$ photocatalytic activity. N and C doped TiO$_2$ showed excellent visible light photocatalytic activity compared to other anion dopants.[64] Compared with N and S doping, the states in the band gap of TiO$_2$ were the deepest for C doping (Fig. 7(a and b)).[62] S-doped TiO$_2$ was extensively investigated and used for VOC purification, introducing S into the TiO$_2$ lattice. The S_{3p} states and O_{2p} of TiO$_2$ can mix, increasing valence bandwidth, and narrowing the TiO$_2$ band gap (Fig. 7(c)). Fig. 8(a and b) illustrates the dopant sites in the structure of a 2 × 2 × 1 supercell consisting of 24 Ti_8O_{16} atoms based on the lattice constants.[63] A number of physical methods or chemical methods, such as sol–gel, hydrolysis, microemulsion, and hydrothermal methods, have been used for the preparation of TiO$_2$ doped with non-metals. N, C, S doping along with non-metal co-doped TiO$_2$ are reviewed in the following sections.

3.1. N doping

N doping attracted extensive attention because it could narrow the TiO$_2$ band gap by creating intra-band-gap states above the VB; electrons could be excited from N impurity levels to the TiO$_2$ CB by N doping, thus enabling visible light absorption.[70] The atomic radius of N is comparable to that of oxygen, and the ionization potential of N is low; therefore, N was prone to enter the TiO$_2$ lattice.[72] Generally, doping with a non-metal whose electronegativity is lower than that of oxygen into the TiO$_2$ lattice can shift the 2p-orbital levels of the VB upward and narrow the band gap. N incorporated into the TiO$_2$ lattice

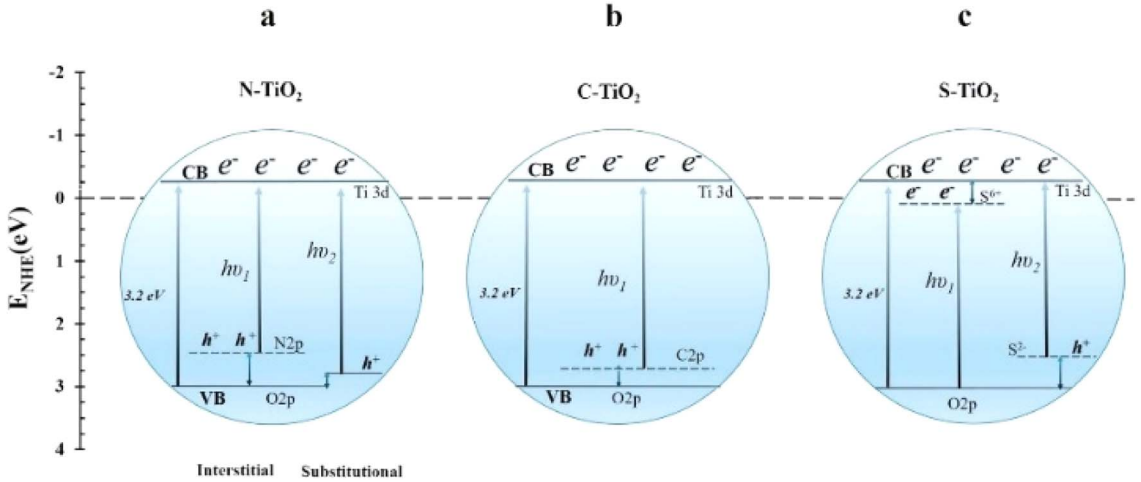

Fig. 7 Schematic of energy levels for (a) N-doped TiO_2, (b) C-doped TiO_2, (c) S-doped TiO_2.[62] Reprinted with permission from ref. 62 Copyright 2018, Elsevier.

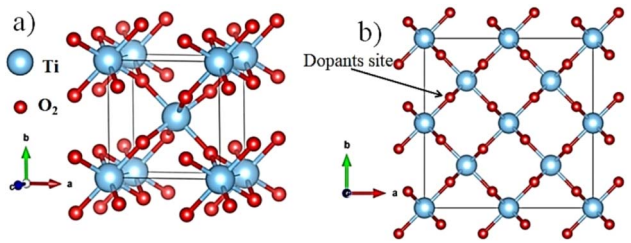

Fig. 8 (a) Crystal structure of rutile TiO_2 and (b) 2 × 2 × 1 supercell of rutile TiO_2.[63] Reprinted with permission from ref. 63 Copyright 2025, Springer Nature.

structure can exist as N^{3-} anions in the form of interstitial states and substitutional states. For substitutional N, the N atom replaced an O atom in the lattice, and the energy of the 2p orbital of N is higher than that of O, thus forming a new impurity level above the top of the valence band or mixing with the 2p orbital of O to shift the valence band upward, significantly enhancing the absorption of visible light. For interstitial N, the N atom is located in the interstitial space of the TiO_2 lattice, and it will also introduce a new energy level into the band gap (usually below the bottom of the conduction band), which could reduce the energy required for electron transition and broaden the light response range. Furthermore, interstitial N often works together with oxygen vacancies, which may be more conducive to charge separation. Substitutional N and interstitial N were the origin of visible light photocatalytic activity for TiO_2 (Fig. 9).[70] The schematics of the electronic band of TiO_2 doped with substitutional N and interstitial N can be seen in Fig. 10.[73] Furthermore, N doping changed the hardness, elastic modulus, refraction index and electrical conductivity of TiO_2.[64]

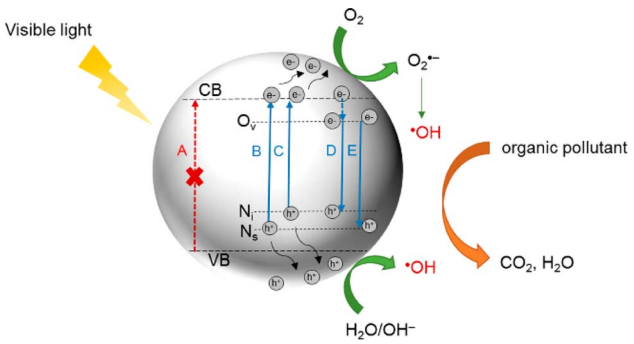

Fig. 9 Effect of N doping on the band structure and visible light photocatalytic activity of TiO_2.[70] Reprinted with permission from ref. 70 Copyright 2021, MDPI.

After baking in an ammonia atmosphere, the binding energy of Ti_{2p} for N–TiO_2 shifted to a lower value, because the electronegativity of N was lower than that of O, after doping TiO_2 with N, and Ti^{4+} was situated in a chemical environment with greater electron cloud density.[72] As for the electronic band structure of N–TiO_2, the highest localized states (acceptor levels) for substitutional and interstitial N were 0.14 eV and 0.73 eV above the VB (Fig. 7(a and c)).[62] For N–TiO_2, three peaks at 396.1 eV, 400 eV, 403.6 eV can be ascribed to N_{1s}. The first peak (396.1 eV) of N_{1s} can be ascribed to substitutional N dopants. The second peak (400 eV) can be ascribed to interstitial N dopants. The third peak (403.6 eV) can be ascribed to NO_x species.[72] N doping can promote the formation of oxygen vacancies in the TiO_2 lattice, since three oxygen atoms can be replaced by two nitrogen atoms to maintain electro-neutrality.[74] The number of surface oxygen vacancies of N–TiO_2 were greater than that of pure TiO_2, and oxygen vacancies could activate O_2 to generate $^{\bullet}O_2^-$. Furthermore, the N–TiO_2 hydroxyl level was stronger than that of pure TiO_2.[72]

Various N-doped TiO_2 were used to photodegrade gaseous formaldehyde,[75] acetaldehyde,[76] acetone,[77] ethylbenzene[78] and toluene,[79] and the photocatalytic activity of photocatalysts under visible light was significantly improved. N–TiO_2 began to deactivate during the photocatalytic reaction. A TiO_2 amorphous layer over N–TiO_2 can improve the photocatalytic stability

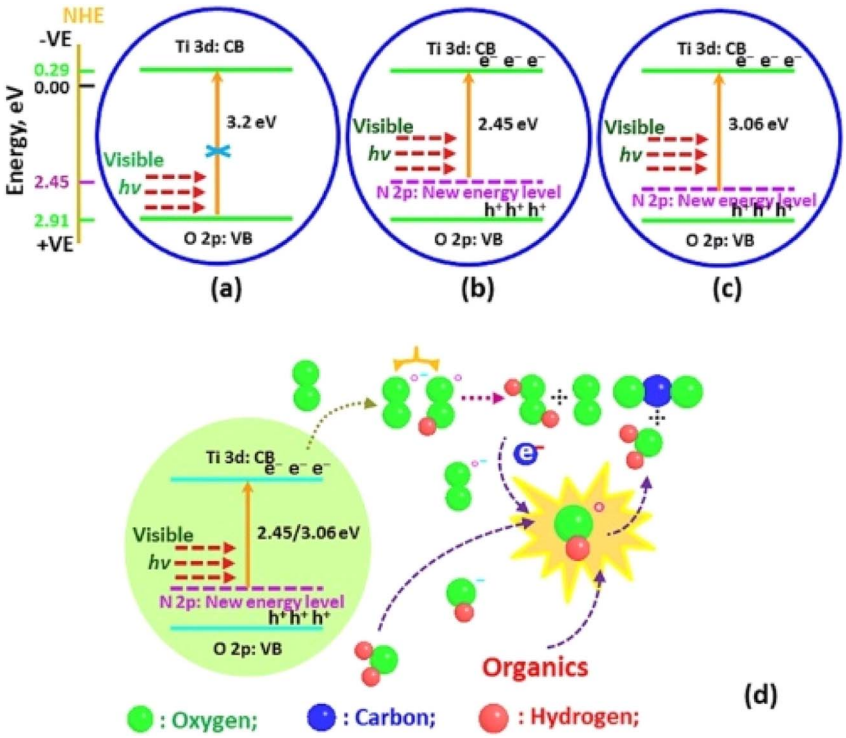

Fig. 10 Energy band gaps of (a) pure TiO_2, (b) N–TiO_2 (interstitial doping), (c) N–TiO_2 (substitutional doping) and (d) the formation mechanism of reactive species during photocatalysis.[71] Reprinted with permission from ref. 71 Copyright 2023, Elsevier.

of the photocatalyst, amorphous TiO_2 can capture photogenerated e^-–h^+ pairs and adsorb O_2, inhibiting the oxidation of lattice nitrogen.[76]

3.2. C doping

For C-doped TiO_2, the lattice oxygen atoms of TiO_2 were partially substituted by carbon atoms. C doping led to the appearance of new impurity energy levels above the VB, which could narrow the band gap, and electrons from the impurity levels were transferred to the TiO_2 CB (Fig. 11),[70] which led to absorption of light with wavelengths below 535 nm.[80] The impurity levels of C-doped TiO_2 shifted upward as the carbon concentration increased, and photogenerated holes showed higher oxidative potential with an increase in carbon concentration.[81] The photocatalytic activity increased with an increase in the electronegativity of the dopant element; C doping was unfavorable for ethylene adsorption, but favorable for $^{\cdot}OH$ formation; ethylene was selectively oxidized to CO_2 by C-doped TiO_2 without deactivation.[81] It was unclear whether the type of carbon doping was interstitial or substitutional; the peak at 280.65 eV (C_{1s} characteristic peak) can be attributed to the Ti–C bond or substitutional carbon doped into the TiO_2 lattice, suggesting the existence of C doping; multiple carbon species, such as carbonate species, substitutional carbon and interstitial carbon, may exist in the lattice of TiO_2 spheres.[80] Furthermore, carbon doping can increase TiO_2 conductivity, accelerating charge transfer from TiO_2 to absorbed VOC molecules.[70] Carbon doping may stabilize anatase TiO_2 and enhance the adsorption capacity of a catalyst for VOCs; C-doped TiO_2 spheres showed superior photocatalytic activity to P25.[80]

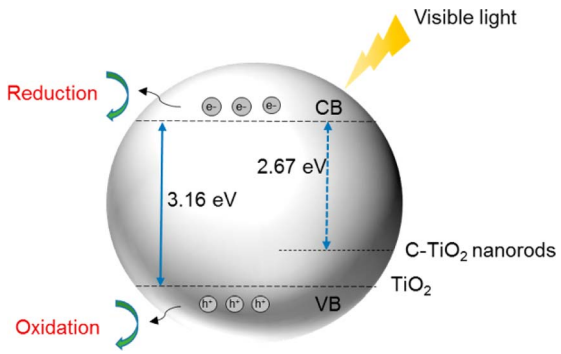

Fig. 11 Schematic of the photocatalytic mechanism of C-doped TiO_2 nanorods with visible light.[70] Reprinted with permission from ref. 70 Copyright 2021, MDPI.

Density functional theory (DFT) calculation was used to study the structural, optical and electronic characteristics of C-doped TiO_2; the substitution of O atoms by C atoms was thermodynamically more favorable, and the substitution was independent of preparation conditions; the impurity levels in the TiO_2 band gap could reduce the gap energy (E_g), thus enhancing the absorbance of visible light.[82] An O atom substituted by a C atom led to great distortion in the structural arrangement around the dopants, changing the electronic and optical properties of TiO_2; a reduction of 0.3 eV was achieved for the band gap.[82] The newly formed electronic levels above the TiO_2 VB were responsible for the narrowed band gap of C-doped TiO_2.

However, lattice defects may form during the process of C doping, which can serve as recombination centers for charge carriers, so it was critical to choose appropriate methods to reduce the amount of TiO_2 lattice defects.

3.3. S doping

S_{3p} states mixing with O_{2p} states of TiO_2 can increase the width of the VB, and incorporating S into TiO_2 lattice can narrow the band gap.[63] The valent states of dopant atoms significantly affected the positions of photogenerated electrons and holes. S^{4+}/S^{6+} cations can substitute Ti^{4+}, while the S^{2-} anion can replace lattice oxygen (Fig. 12).[67] Cationic S doping can improve charge separation[83] and extend the TiO_2 absorption spectrum region to visible light,[84] so cationic S doping was a facile method to improve TiO_2 photocatalytic activity. The ion atomic radius of Ti^{4+} (0.64 Å) is significantly greater than that of S^{6+} (0.29 Å), so S^{6+} substituting for Ti^{4+} may decrease the TiO_2 crystal size.[67] After substitution of S^{6+} for Ti^{4+}, S_{3s} orbitals created states which were above the O_{2p} orbitals of the TiO_2 VB, while S_{3p} orbitals contributed to the lowered TiO_2 CB.[63] Anionic S doping was more difficult to realize than cationic S, because the S^{2-} ionic radius (1.7 Å) is notably larger than that of O^{2-} (1.22 Å).[83] Therefore, a Ti–S bond required higher formation energy than a Ti–O bond.

Some other researchers reported that TiO_2 doping by replacing Ti with S^{4+} and S^{6+} was unfavorable for TiO_2 bulk but favorable for the TiO_2 surface; the reports of strong absorption of visible light by S-doped TiO_2 may be ascribed to other impurities, such as N, C or Ti^{3+}.[84] Novel theoretical models were used to analyze S^{4+} and S^{6+} doping in different surface and bulk positions of TiO_2. S preserved its typical coordination geometries in S-doped TiO_2: a trigonal pyramid for S^{4+} but a tetrahedron for S^{6+}. For S^{4+}-doped TiO_2, the band gap decreased from 3.22 eV to 2.65 eV, while for S^{6+}-doped TiO_2, the band gap decreased from 3.22 eV to 2.96 eV. The maximum amount of S^{6+} was observed with the ratio S^{6+}/S^{4+} being about 5.61 with 9% S atoms, indicating that S in the catalyst was in the form of cations; the presence of S^{6+} in TiO_2 improved visible light photocatalytic activity and reduced the band-gap energy; in addition, S^{6+}/S^{4+} can act as an electron capture agent, improving the electrical conductivity of the photocatalyst and accelerating the transfer of electrons and holes; compared with pure TiO_2, S-doped TiO_2 showed improved photoactivity for acetaldehyde degradation under visible-light irradiation.[85]

Thiourea and CS_2 were used as sulfur precursors, and cationic S and anionic S were doped into the TiO_2 lattice. As for the cationic precursor, Ti^{4+} can be substituted by S^{6+}, forming a Ti–O–S bond. The charges between sulfur and oxygen atoms should maintain a balance; therefore, the created hydroxide eventually neutralized the extra positive charges. For the anionic precursor, an O–Ti–S bond appeared in S–TiO_2, and O atoms in the O–Ti–O network were partially replaced by S atoms; it was noted that anionic S^{2-} existed mainly in the lattice of TiO_2, while cationic S, such as SO_4^{2-}, was mainly chemisorbed on the TiO_2 surface due to the calcination process.[63] S-doped TiO_2 using thiourea (S^{2-}) as the source shifted the absorption to the visible spectrum region and enabled photocatalytic activity under visible light; compared with TiO_2, S-doped TiO_2 was significantly more active for acetaldehyde degradation under visible light irradiation.[86]

4. Metal and non-metal co-doping

Metal and non-metal co-doping was considered a way to solve the problems existing in single-doped TiO_2. Doping metal and non-metal into the TiO_2 lattice can produce doping energy levels in the TiO_2 band gap (Fig. 13). As for doping, metal components usually substituted Ti sites in the TiO_2 lattice to form dopant levels near the CB, while non-metal components usually formed new dopant levels close to the TiO_2 VB, which reduced the band gap and led to the absorption of visible light; co-doping of TiO_2 showed lower band-gap energy values than single-doped TiO_2; and the synergistic effects of metal and non-metal co-doping also promoted the separation of electrons and holes.[27] Furthermore, co-doping can decrease crystallite size and increase the specific surface area of TiO_2.[87] It was crucial to find appropriate dopants and the optimum amounts of dopants. TiO_2 co-doped with metal/metal, metal/non-metal and non-metal/non-metal are discussed in the following sections.

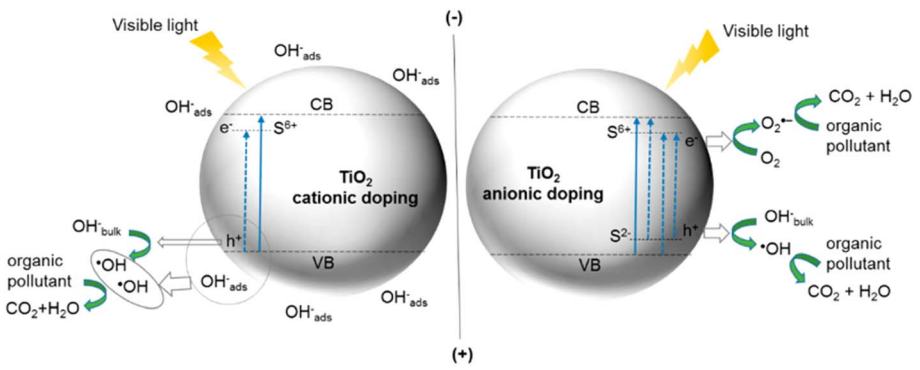

Fig. 12 Schematic of the PCO mechanism of TiO_2 doped with cationic and anionic S.[70] Reprinted with permission from ref. 70 Copyright 2021, MDPI.

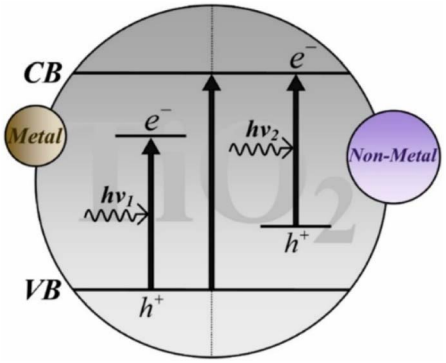

Fig. 13 The mechanism of TiO_2 photocatalysts co-doped by metal and non-metal dopants.[27] Reprinted with permission from ref. 27 Copyright 2024, Elsevier.

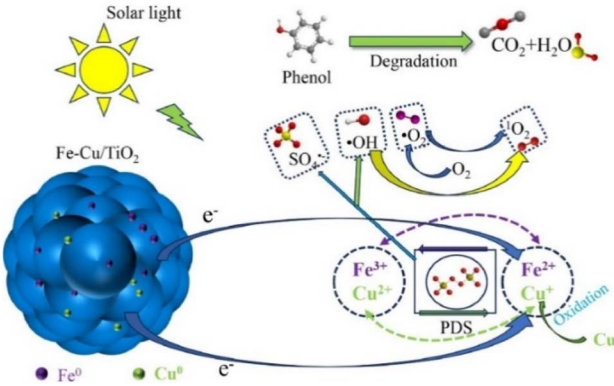

Fig. 15 Mechanistic diagram of the synergistic degradation of phenol by Fe–Cu/TiO_2 composites.[89] Reprinted with permission from ref. 89 Copyright 2024, Elsevier.

4.1. Metal co-doping

The doping mechanism and physiochemical properties of TiO_2 doped with two different metals have not yet been investigated in depth. New energy levels were formed in Mn/FeTNT@Ti-500 due to doping with Fe^{2+}, Fe^{3+}, Mn^{2+} and Mn^{3+} ions. The trapped states involving Fe^{3+}/Fe^{2+} formed below the conduction band, while Fe^{3+}/Fe^{4+} trapped states formed above the valence band.[88] As shown in Fig. 14, Mn^{3+}/Mn^{2+} also acted as an electron trap site, while the Fe^{3+}/Fe^{4+} site above the TiO_2 valence band acted as a hole trapping site. These trapped holes were immediately released because of the reduction of unstable Fe^{4+} to stable Fe^{3+} ions; thereafter, these holes migrated to the surface and oxidized adsorbed H_2O molecules.[88] As the standard redox potential for Cu^{2+}/Cu^{+} (0.17 V) is lower than that for Fe^{3+}/Fe^{2+} (0.77 V), Cu^{+} can easily reduce Fe^{3+} to Fe^{2+}; therefore, Fe^{2+} can be regenerated on the TiO_2 surface (Fig. 15), promoting Cu^{2+}/Cu^{+} and Fe^{3+}/Fe^{2+} cycles and further promoting ROS generation.[89]

The Ag^{+} ion radius (1.26 Å) is much bigger than that of Ti^{4+} (0.74 Å). The ion radius of V^{4+} (0.72 Å) is similar to that of Ti^{4+} (0.74 Å); therefore, V^{4+} can substitute Ti^{4+} and form a Ti–O–V bond in the TiO_2 lattice. Both Ag^{+} and V^{4+} can be incorporated into the TiO_2 lattice, which may reduce Ti^{4+} to Ti^{3+}. Consequently, the ratio of Ti^{3+}/Ti^{4+} for TiO_2 co-doped with Ag and V was higher than that for V or Ag singly-doped TiO_2, Ag and V co-doping promoted doping into the TiO_2 lattice, which was favorable for oxygen vacancy formation in TiO_2 (or Ti^{3+} formation). The incorporation of Ti^{3+} and V^{4+} into the TiO_2 lattice can act as intermediate agents for internal electron transfer; the Ag_2O band-gap energy (1.3 eV) was lower than that of V_2O_5 (2.3 eV); and the energy needed for internal electron transfer for Ag–TiO_2 was lower than that for V–TiO_2.[87] In addition, many different Fermi levels existed for metallic Ag; Ag can facilitate internal electron transfer by Ag_2O; V can facilitate internal electron transfer in the TiO_2 lattice; and they can also facilitate exterior electron transfer among Ag, Ag_2O and TiO_2 in Ag–TiO_2.[87] Furthermore, Ag, Ag_2O, and V_2O_5 agglomeration could be hindered in Ag and V co-doped TiO_2.[87]

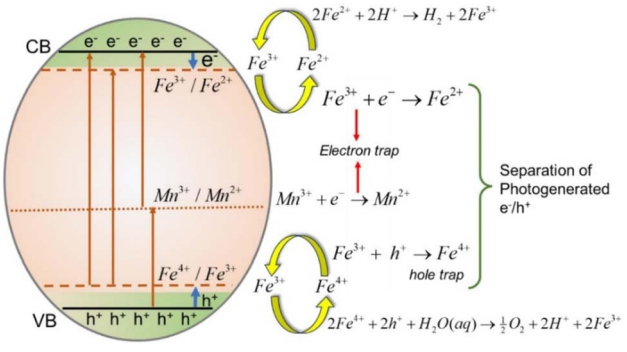

Fig. 14 Schematics of the charge transfer process of photocarriers in a Mn/Fe-TNT@Ti-500 photocatalyst.[88] Reprinted with permission from ref. 88 Copyright 2024, Elsevier.

For Ag-doped TiO_2/PU, the removal efficiency and degree of mineralization of *n*-hexane were 87.2% and 92.1%, while the removal efficiency and degree of mineralization of *n*-butyl acetate were 90.1% and 94.3%. For V-doped TiO_2/PU, the removal efficiency and degree of mineralization of *n*-hexane were 82.6% and 91.1%, while the removal efficiency and degree of mineralization of *n*-butyl acetate were 84.7% and 92.7%. For Ag and V co-doped TiO_2/PU, the removal efficiency and degree of mineralization of *n*-hexane were 93.7% and 93.2%, while the removal efficiency and degree of mineralization of *n*-butyl acetate were 95.5% and 96.2%.[87] Ag@V–TiO_2/PU showed advantages of both Ag and V, and exhibited excellent photocatalytic degradation performance for a hexane and butyl acetate mixture.[87]

Bi and Zn co-doped TiO_2 was used for the photocatalytic degradation of toluene, and moderate Bi–Zn co-doping levels were significantly favorable for toluene photodegradation under visible light irradiation.[90] Doping Bi into the TiO_2 lattice can generate a new doped energy level below the TiO_2 CB edge, and electrons excited from the TiO_2 VB to Bi orbitals led to a decrease in the band gap. Zn^{2+} was not incorporated into the TiO_2 lattice and formed ZnO crystallites, which were distributed mainly on the interface of TiO_2, and it acted as a mediator for interfacial charge transfer and hindered electron–hole

recombination. These synergistic effects were responsible for enhanced photocatalytic performance. Under visible light irradiation, electrons were excited at the TiO_2 (R) VB and transferred to the Bi energy level; then they shifted to the CB of TiO_2 (R) (−0.48 eV *vs.* SHE), ZnO (−0.15 eV) and TiO_2 (A) (−0.13 eV); electrons transferred along the gradient of the CB edge potential (Fig. 15).[95] Toluene degradation efficiencies over $TiBi_{1.9\%}O_2$ and $TiBi_{1.9\%}Zn_{1\%}O_2$ were 51% and 93%, much higher than the 25% for TiO_2.[90]

4.2. Non-metal co-doping

C and N co-doped TiO_2 combined the advantages of C-doped and N-doped TiO_2. The incorporated C atoms can form carbonaceous species I, which can serve as photosensitizer (C*).[70] After excitation of carbonaceous species I, electrons were injected into the TiO_2 CB; these electrons could be further transferred to O_2 adsorbed on the TiO_2 surface, forming $^{\bullet}O_2^-$, which could subsequently generate H_2O_2 and $^{\bullet}OH$, combining with $^{\bullet}OH$, and participating in pollutant degradation (Fig. 16).[70] C doping can also enhance the adsorption capacity of TiO_2 for pollutants. N doping can create an intra-band-gap state (IB) above the VB, narrowing the band gap.[70] The synergistic effect of N and C co-doping can further decrease the band-gap energy of C,N-co-doped TiO_2 to 2.80 eV. C and N can be co-doped into TiO_2 by various carbon and nitrogen sources, such as ETA, DEA and TELA. The N 1s peak in the range of *ca.* 396–402 eV can be ascribed to the existence of O–Ti–N bonds, suggesting the incorporation of substitutional N into the TiO_2 lattice.[70] The peaks from 284.6 to 289.6 eV were attributed to the existence of carbon; the peaks at 285.9–286.7 eV and 288.5–288.7 eV were mainly attributed to C–O and C=O bonds; the peaks at 288.0–288.9 eV could be ascribed to Ti–O–C bonds.[70]

N and S co-doping can reduce the band gap of TiO_2 because of the generation of additional impurity levels.[64] N doping can form a delocalized state in the TiO_2 band gap, which increases visible light absorption. S doping facilitates the adsorption of organic species onto the surface of N and S co-doped TiO_2. The improved photocatalytic degradation efficiency can be ascribed to the following reasons:[74] (1) inhibition of the recombination of electron–hole pairs; (2) the generation of impure electronic states narrowing the band gap; (3) interfacial bonding; (4) defective sites; (5) a change in textural characteristics. Thiourea was usually used as an S source, and urea and ammonium nitrate were usually used as an N source; some chemical reagents can be used as both N and S source, such as ammonium sulfate and ammonium thiocyanate.[70] N and F co-doped TiO_2 was also used for the degradation of gaseous ethylbenzene; N doping promoted the generation of $^{\bullet}O_2^-$ over TiO_2 oxygen vacancy sites under visible light irradiation; F doping can generate new active sites and facilitate the generation of $^{\bullet}OH$; conversion rates of ethylbenzene for undoped, N-doped, and N and F co-doped TiO_2 were 0%, 13.5%, and 17.0%, respectively, under visible light.[91]

Tri-doping was an efficient method to improve TiO_2 visible light photocatalytic activity. C, N, and S co-doping can form new impurity levels, including N_{2p}, S_{2p} and C_{1s} (Fig. 17); the carbon atom served as a photosensitizer under visible light irradiation, while N and S doping led to a mixture of N_{2p} and S_{2p} orbitals with O_{2p} orbitals in TiO_2;[70] and the band gap was narrowed compared to pure TiO_2. In the XPS spectra for N, S and C tri-doped TiO_2, N can be ascribed to Ti–O–N and Ti–N bonds, S can be mainly ascribed to the Ti–O–S bond, and C can be attributed to the Ti–O–C bond.[92] C,N,S-tri-doped TiO_2 nanosheets exposing {001} facets exhibited excellent photocatalytic activity.[93]

4.3. Metal and non-metal co-doping

Metal and nonmetal co-doping combined the advantages and overcame some drawbacks of single doping. The synergistic effects of metal and non-metal co-doping facilitated the separation of electrons and holes, and enhanced the visible light photocatalytic activity of TiO_2. Metal dopants were easy to substitute for Ti sites in the TiO_2 lattice to generate dopant levels near the CB, and metal ions could act as a mediator for interfacial charge transfer and hinder electron–hole pair recombination due to the enhancement in quantum efficiency for co-doped TiO_2.[90] Non-metal dopants potentially formed new levels close to the VB, which reduced the band gap and led to the absorption of visible light. Non-metal and transition metal co-doping was a feasible method to improve TiO_2 photocatalytic

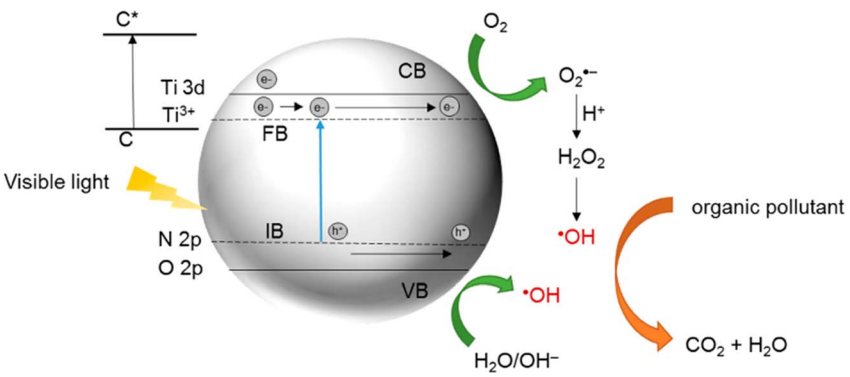

Fig. 16 Schematic of the mechanism for C,N-co-doped TiO_2 photocatalysis under visible light.[70] Reprinted with permission from ref. 70 Copyright 2021, MDPI.

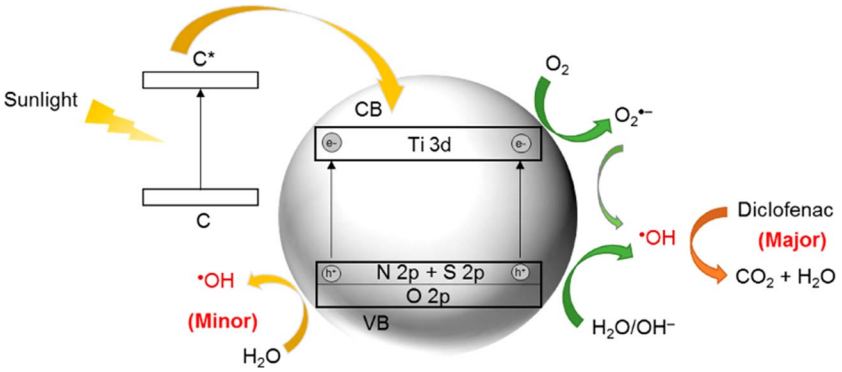

Fig. 17 Schematic for the improvement of photocatalytic activity over C,S,N-tri-doped TiO_2.[70] Reprinted with permission from ref. 70 Copyright 2021, MDPI.

activity. Fe, Zn, Cu, Cr combined with N co-doped TiO_2 showed improved photocatalytic activity under visible light.[96] The photocatalytic activity of N-doped TiO_2 could be further enhanced by W^{4+} (Fig. 18) or Fe^{3+} co-doping. Photogenerated holes can oxidize the lattice nitrogen of N-doped TiO_2, and nitrogen is gradually lost; however, Fe-ion doping could improve the stability of N-doped TiO_2.[97] Furthermore, N and Fe co-doping could hinder the transformation of anatase to rutile. The removal efficiency of *p*-nitrophenol for Fe-doped, N-doped, and Fe and N co-doped TiO_2 were about 47%, 41%, and 67%, respectively.[97]

Different preparation methods may dope ions into different positions of the TiO_2 crystal lattice.[98] The position and structure of dopant elements significantly affected the electronic, optical, structural characteristics of TiO_2.[73] Based on the doping sites and relative positions of the dopants, the network of Fe and N co-doped TiO_2 was modeled with three configurations (Fig. 19).[94] In Model A, Fe atoms and N atoms were doped at Ti and N sites, and the distance between Fe atoms and N atoms was 1.739 Å. In Model B, Ti atoms were replaced by Fe atoms, O atoms were replaced by N atoms, and the distance between Fe atoms and N atoms was 7.805 Å. In Model C, two N atoms (at a distance of 2.21 Å) were inserted at the interstitial sites, Fe was located at the Ti site of a $3 \times 2 \times 1$ supercell, and DFT calculation was applied to study the influence of dopant location on band structure and the enhancement of visible light absorption of mono-doped and co-doped TiO_2.[94] After iron oxide was loaded into N-doped TiO_2, the heterogeneous electrons transferred from $TiO_{2-x}N_y$ to Fe_2O_3, promoting the effective separation of photoinduced electrons and holes; furthermore, the electrons can be excited and transferred by various pathways from the VB to the CB after co-doping, enhancing the visible light photocatalytic activity of N/Fe co-doped TiO_2.[73] However, a negative effect on photocatalytic activity for TiO_2 co-doping with Fe was also observed, which could be due to the formation of anion vacancies in co-doped TiO_2 for charge compensation.

5. Surface and interface design

Photodegradation reactions occurred on the catalyst surface, and the surface and interface structure and properties of catalysts (like crystallite size, crystalline phases, pore structure, specific surface area, active sites and adsorption performance) greatly influenced heterogeneous photocatalytic reactions. The interface structure influenced interfacial charge transfer and recombination; furthermore, the surface structure affected the generation of reactive radicals, so they significantly affected the removal efficiency of gaseous VOCs.[26] Interfacial charge separation and transfer occurred at the interface of semiconductors

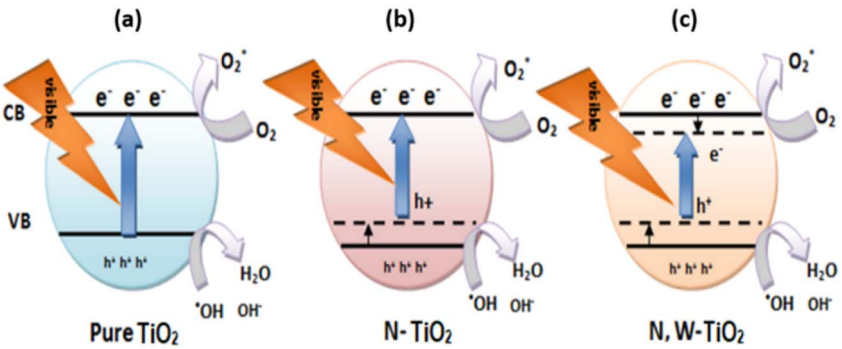

Fig. 18 Proposed pathway for photocatalytic degradation over (a) undoped TiO_2; (b) TiO_2 doped with N; (c) TiO_2 co-doped with N and W.[95] Reprinted with permission from ref. 95 Copyright 2022, MDPI.

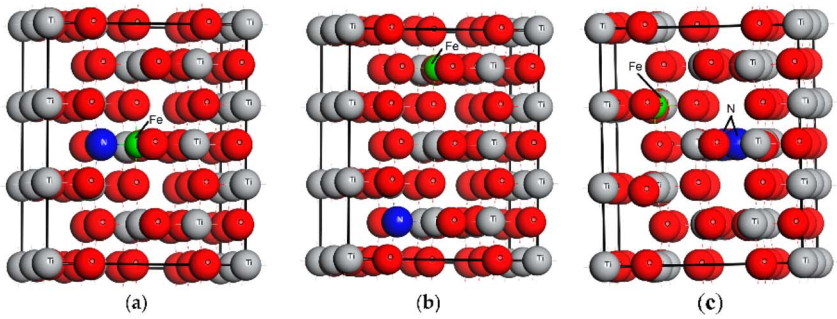

Fig. 19 Relative positions of Fe and N dopants in the TiO_2 lattice: Model A (a), Model B (b), and Model C (c).[94] Reprinted with permission from ref. 94 Copyright 2018, MDPI.

and organic compounds; interfacial charges may directly oxidize or reduce VOCs or form reactive oxidants like superoxides and hydroxyl radicals.[99] The surface and interface design of TiO_2 can promote charge carrier separation, hinder charge carrier recombination and shift the optical absorption to visible light.

5.1. Construction of oxygen vacancy

The loss of lattice oxygen led to the generation of oxygen vacancies (OVs), which could increase active sites; the TiO_2 lattice OVs can be seen in Fig. 20.[102] After doping with Ni^{2+}, two Ti atoms were substituted by two Ni atoms to keep the concentration of Ni similar to the experimental doped concentration of Ni (Fig. 20). It was reported that the insertion of one OV subsequently introduced two Ti^{3+} defects into the Ni-doped TiO_2 supercell.[100] At present, many methods have been used to construct OVs, such as ultraviolet induction,[103] laser ablation,[104] annealing,[101] reductant addition,[105] and doping.[106] OVs significantly influence the photocatalytic degradation of VOCs. Firstly, OVs could influence mobility of surface lattice oxygen and provide coordinated sites for molecule activation, thus activating the gas molecules.[107] Secondly, surface OVs can capture electrons or holes and facilitate the transfer of charge carriers to the adsorbate, thus greatly influencing the dynamics of charge carrier transfer. Thirdly, oxygen defects generally adjusted the electronic state *via* local electrons and the coordination structure of the adsorbate *via* hanging bonds,[101] promoting charge carrier transport, and hindering the recombination of electrons and holes.[107] Fourthly, OVs over the TiO_2 surface provided the primary adsorption sites for VOC molecules,[108] improving the adsorption capacity of TiO_2 for VOCs.

OVs can reduce the adsorption energy and activation barrier of O_2, which is beneficial for the formation of $^{\bullet}O_2^-$; OVs can also promote the disintegration of H_2O to $^{\bullet}OH$.[109] However, O_2 and H_2O molecules can be easily adsorbed on the surface of OV sites, so the structural stability of surface OVs was poor. Constructing subsurface defects and decorating metal nanoparticles were used to improve the stability of surface OVs.[62] OVs created on the surface of TiO_2 facilitated the incorporation of O atoms from O_2 into phenol, because OVs could effectively suppress the single-electron reduction of O_2 to form $^{\bullet}O_2^-$, and promote the two-electron reduction process instead, which was typically associated with the generation of H_2O_2; and the generated H_2O_2 could (in some cases) provide additional $^{\bullet}OH$ to drive the benzene hydroxylation reaction (Fig. 21).[101]

Annealing temperature was used to adjust the concentration of surface OVs, and photocurrent and photoluminescence measurements suggested that the existence of interfacial OVs promoted interfacial electron transfer; surface OVs promoted the adsorption and activation of toluene and O_2, facilitating the formation of intermediates and enhancing the mineralization efficiency for toluene.[110] Ru/TiO_x with abundant OVs showed

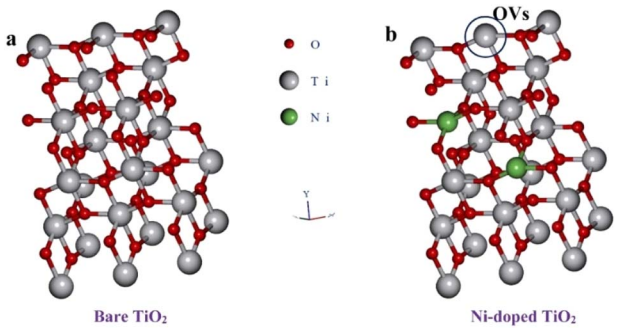

Fig. 20 Anatase TiO_2 (101) supercell (2 × 2 × 1) models for (a) pure TiO_2 (16Ti and 32O atoms) and (b) Ni-doped TiO_2 (14Ti, 31O and 2Ni atoms).[100] Reprinted with permission from ref. 100 Copyright 2025, Elsevier.

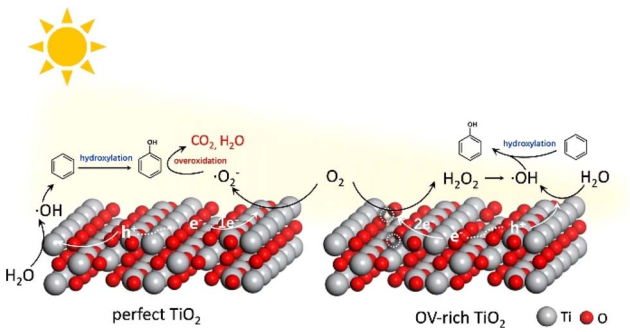

Fig. 21 Potential reaction pathways for the photocatalytic oxidation of benzene to phenol over pristine TiO_2 and OV-rich TiO_2.[101] Reprinted with permission from ref. 101 Copyright 2025, John Wiley and Sons.

excellent catalytic performance for 1,2-DCE and toluene oxidation; Ru/TiO_x greatly inhibited the formation of intermediate byproducts and Cl_2; most OVs of Ru/TiO_x were still retained after use; and the catalysts with OVs were more suitable and promising for the oxidative removal of multicomponent VOCs.[107] However, surface OVs in TiO_2 can also serve as electron and hole recombination centers, which is adverse for photocatalysis.[111]

5.2. Facet engineering

Different lattice planes of TiO_2 showed different activities; exposing different facets could influence VOC degradation paths, and exposing highly active facets could enhance photocatalytic activity.[42] The design of a facet was a feasible method to improve TiO_2 photocatalytic activity. Although the role of the facets was controversial, some studies indicated that exposing particular facets can enhance the selectivity of VOC photocatalytic degradation, and partial facets showed higher adsorption capacity for VOC molecules.[29] Anatase nanosheets, such as rectangular, octahedral, and decahedral shape structures, exposed different ratios of (001), (101) and (100) facets; the exposed facets affected their photocatalytic activity, especially in terms of mineralization efficiency and degradation pathways.[114]

Experiments combining computational methods were used to study the attack on the phenyl ring by $^{\bullet}OH$ and $^{\bullet}O_2^-$: the increased distance of adjacent sites was favorable to facilitate the attack by $^{\bullet}O_2^-$ on the para position; so the surface structure may significantly influence the formation of products.[114] Different TiO_2 nanostructures, such as nanotubes, nanorods, nanofibers, nanospheres, and nanosheets with different exposed facets, were produced and showed different photocatalytic activity for VOC degradation.[118] The respective functions of different crystal facets were explored in the reaction, as shown in Fig. 22(a–e). Photodeposited Au particles generated by $AuCl_4^-$ reduction were distributed mainly on the (101) facet; while the photodeposited MnO_x formed by Mn^{2+} oxidation was predominantly distributed on the (001) facet, indicating that the photogenerated electrons tended to accumulate on the (101) facet, causing a reduction reaction; whereas photogenerated holes migrated preferentially to the (001) facet, causing an oxidation reaction; therefore, *p*-xylene was activated mainly on the (001) facet, while O_2 was activated predominantly on the (101) facet (Fig. 22(f)).[112]

Crystal planes with higher stability were preferentially exposed. TiO_2 with particular facets exposed can be achieved by reducing the surface energy. It had been proved that the anatase TiO_2 (001) facet showed higher photoreactivity. F-capping could induce the growth of a TiO_2 crystal along a specific axis, which led to the formation of particularly reactive (001) facets in anatase TiO_2. TiO_2 surface termination with F atoms led to the exposure of more (001) facets, and the percentage of (001) facets could be predicted if *c* values were provided.[115] Adsorbed HF can create additional energy bands in the primordial band gap of pure anatase TiO_2, such as Ti^{3+} d-bands, narrowing the band gap.[116] The residual fluoride adsorbed on the TiO_2 surface can form bonds with Ti atoms, improving the adsorption performance for O_2 and promoting charge carrier separation: the adsorption capacity of TiO_2 (001) facets for phenol was 1.68 times that of polycrystalline TiO_2, and the oxidation rate on the

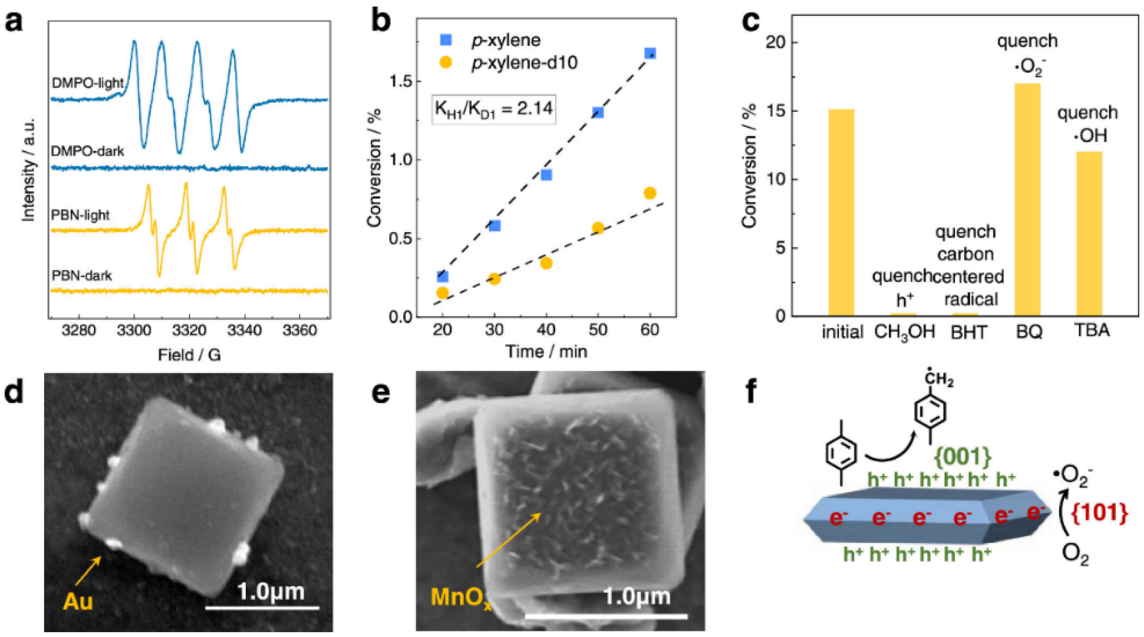

Fig. 22 (a) *In situ* EPR spectra of $^{\bullet}O_2^{2-}$ and carbon-centered radicals on (001)-exposed TiO_2. (b) KIE experiments of *p*-xylene photooxidation on (001)-exposed TiO_2. (c) The conversion of *p*-xylene in the presence of O_2 with the addition of scavengers contrasted to the general condition. SEM images of *in situ* photodeposited Au (d) and MnO_x (e) on TiO_2. (f) Schematic diagram of charge distribution on TiO_2 under irradiation.[112] Reprinted with permission from ref. 112 Copyright 2024, American Chemical Society.

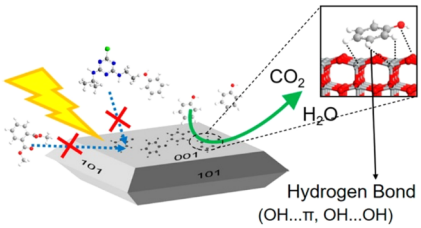

Fig. 23 Schematic diagram of phenol photocatalytic oxidation on 001-MI-TiO_2.[113] Reprinted with permission from ref. 113 Copyright 2020, American Chemical Society.

TiO_2 (001) facet was 12.93 times that of polycrystalline TiO_2.[117] The significantly increased removal of phenol could be ascribed to enhanced adsorption and photocatalytic performance (Fig. 23).[113]

5.3. Pore structure and specific surface area

The specific surface and pore structure significantly influenced photocatalytic activity, and the design of the specific surface area and pore structure of TiO_2 was a feasible method to enhance VOC photocatalytic degradation efficiency. There were many methods for preparing photocatalysts with high specific surface area and ideal pore structure, such as the hydrothermal method,[120] template method,[121] and anodic oxidation method,[122] and the template method was the most widely used. Pore structures, like macropores and mesopores, can hinder the agglomeration of photocatalysts and facilitate mass transfer, which can facilitate VOC molecules to make adequate contact with photocatalysts. Furthermore, the pore structure can also shorten the transmission distance of charge carriers, which is favorable for the separation of electrons and holes. Mesoporous TiO_2 was used for the photocatalytic degradation of xylenes: compared to TiO_2 nanoparticles, mesoporous TiO_2 showed better photocatalytic activity and stability.[123] The preparation route for a hierarchical flower-like Ag_3PO_4/TiO_2 heterojunction can be seen in Fig. 24. 0D/3D hierarchical Ag_3PO_4/TiO_2 showed excellent photocatalytic performance under solar light irradiation, which could be due to its unique hierarchical porous structure, suitable size of Ag_3PO_4, the formation of type-II heterojunctions, and the high separation efficiency of photo-induced carriers.[119]

Generally, photocatalysts with larger specific surface areas provided more active sites, generating more active free radicals, which can decompose interacted VOC molecules. Specific surface area was related to the mean particle size of TiO_2: the particle size significantly affected TiO_2 photocatalytic performance, the specific surface area of TiO_2 nanoparticles was three times that of P25, and they showed excellent photocatalytic degradation efficiency. Trimesoyl chloride–melamine copolymer and TiO_2 nanocomposites were applied for the photocatalytic degradation of gas-phase benzene under visible light; the amide bonds of TMP decreased the size of TiO_2 nanoparticles, thus increasing the specific surface area of the photocatalysts, and the degradation efficiency for (TMP)-TiO_2, unmodified TiO_2 and P25 were 100%, 19% and 23.6%, respectively.[124] Titania microballs with different exposed facets (Fig. 25) composed of faceted nanoparticles were used for various photocatalytic applications, because of their high activity for both reduction and oxidation reactions and large size (favourable for recycling and commercialization).[120] The enhanced photocatalytic activity could be ascribed to mesoporous structure, higher specific surface area, extended light absorption and shortened mass transfer distance due to a thinner hollow shell structure with abundant pore channels.

5.4. Surface halogenation

Surface halogenation was related to the incorporation of halogens (F, Cl, Br, I) onto the surface of the photocatalyst to improve surface properties. The introduced H_2O molecules interacted with holes to generate $^{\cdot}OH$; at the same time, H_2O molecules would compete for adsorption sites with VOC molecules, which was adverse for VOC degradation.[29] Surface halogenation could adjust the surface hydrophilicity of photocatalysts. Surface fluorination was favorable for the generation of free $^{\cdot}OH$, although surface fluorination was adverse for TiO_2 to adsorb acetaldehyde; it would enhance the first-order rate constant for CO_2 production by 2.5 times.[125]

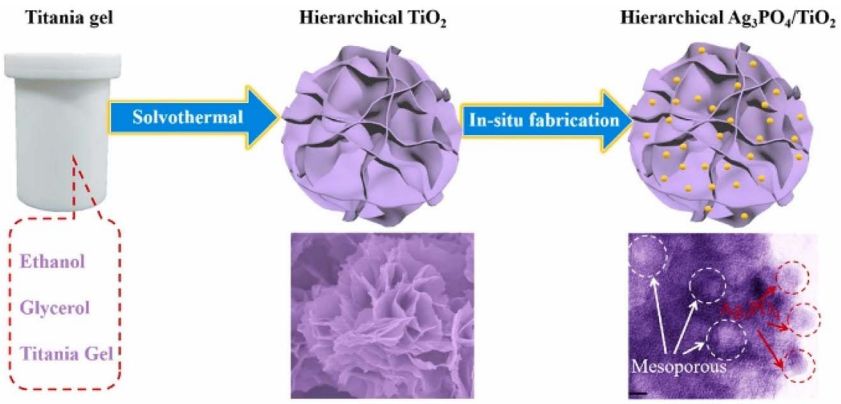

Fig. 24 Schematic of the prepared hierarchical flower-like Ag_3PO_4/TiO_2 heterojunction.[119] Reprinted with permission from ref. 119 Copyright 2022, Elsevier.

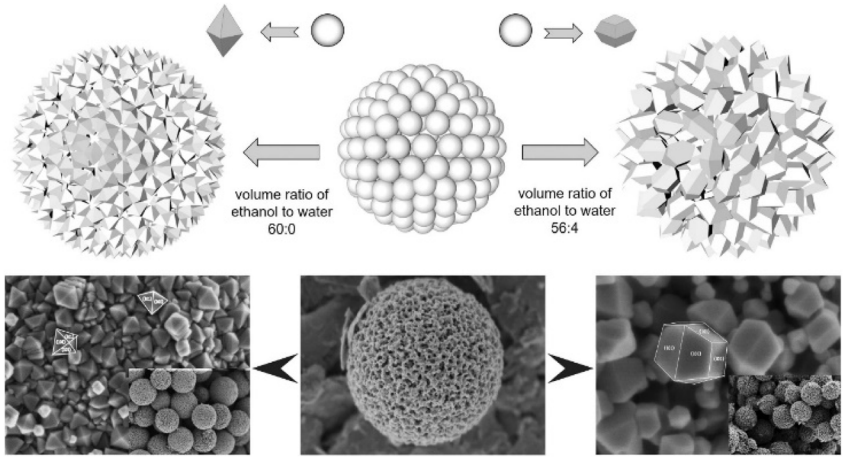

Fig. 25 (Top) Schematic illustration for the formation of a mesoporous microball composed of faceted anatase nanocrystals; (Bottom) respective FE-SEM images.[120] Reprinted with permission from ref. 120 Copyright 2024, Elsevier.

Surface-fluorination can also stabilize the (001) facets and promote the formation of anatase TiO_2 nanosheets.[126]

As shown in Fig. 26, the O_2 adsorption energy, E_{ads}, for photocatalysts can be ordered as follows: TiO_2 (−0.346 eV) < F–TiO_2 (−0.607 eV) < TiO_{2-x} (−1.928 eV) < F–TiO_{2-x}(OV) (−1.956 eV) < F–TiO_{2-x}(FD) (−2.431 eV), indicating that F–TiO_{2-x} had the strongest O_2 adsorption capacity, and both F and OVs were favourable for oxygen adsorption. The ordered ability of O_2 molecules to accept electrons was: F–TiO_2 (0.03 eV) < TiO_2 (−0.11 eV) < F–TiO_{2-x}(OV) (−0.37 eV) < F–TiO_{2-x}(FD) (−0.40 eV) < TiO_{2-x} (−0.57 eV). Although the electron transfer ability and activation of O_2 molecules over F–TiO_{2-x} were lower than those of TiO_{2-x}, F–TiO_{2-x} (with more F-substituted oxygen sites and OVs) could adsorb more O_2 molecules, which could increase the generation of $^{\bullet}O_2^-$ and $^1O_2$.[29] After TiO_2 fluorination, the adsorption capacity for toluene was enhanced by about two times under three different humidity conditions.[29] The total photocatalytic activity would also eventually be increased.

Many different explanations have been proposed to explain the surface fluorination mechanism to improve photocatalytic activity. Some studies proved that more $^{\bullet}OH$ can be produced over surface-fluorinated TiO_2.[127] However, some studies proposed that surface fluorination can form Ti–F bonds on the TiO_2 surface, which can hinder the recombination of photogenerated electrons and holes.[69] F-modified TiO_2 was prepared *via* a plasma method; lattice F, ≡Ti–F bonds, and oxygen defects were found in F-doped TiO_2; ≡Ti–F bonds can efficiently facilitate the separation of electrons and holes, boost the production of $^{\bullet}O_2^-$ and $^{\bullet}OH$, and the band gap for treated TiO_2 can be reduced to 2.78 eV after lattice F doping.[128] However, excessive fluorination induced structural defects, which can serve as recombination centers for electrons and holes and hinder the transfer of interfacial electrons.

Besides surface fluorination, chlorination, bromination and iodination can also affect the photocatalytic activity of TiO_2. Three halogen hydric acids (HF, HCl and HBr) were used to

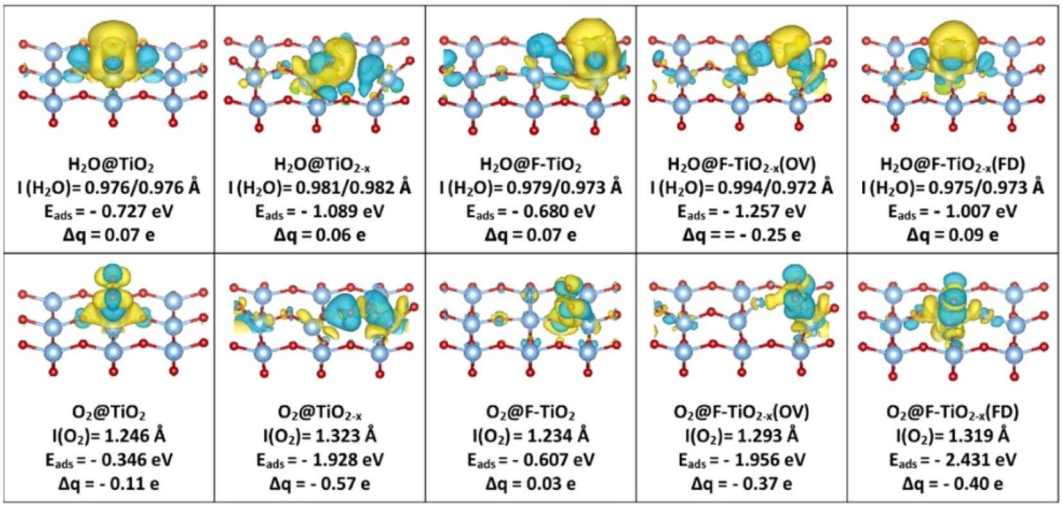

Fig. 26 Calculated adsorption and activation of O_2 and H_2O molecules on fluorinated TiO_2.[29] Reprinted with permission from ref. 29 Copyright 2022, Elsevier.

synthesize mesoporous TiO_2 nanosheets.[129] F, Cl or Br species on the surface of TiO_2 were confirmed by XPS; the kinds of halogenated acid affected the composition of crystalline phases: 100% anatase for TiO_2–I(HF), anatase/rutile phases for TiO_2–I(HCl), anatase/brookite phases for TiO_2–I(HBr).[129] Surface halogenation can narrow the band gap and lead to a red shift of the absorption edge, from 395 nm to 517 nm; with an increase in Br doping content, the band gap of Br–TiO_2 hollow spheres reduced from 2.85 eV to 1.75 eV; doping with an appropriate content of Br significantly improved the photocatalytic activity.[130] All in all, appropriate surface halogenation can improve TiO_2 photocatalytic activity.

5.5. Construction of a heterojunction

A heterojunction semiconductor can be obtained by coupling a semiconductor with another material, such as noble metals or other semiconductors. Many semiconductors have been used for the construction of heterojunctions, such as CdS,[133] ZnO,[134] SnO_2,[135] WO_3,[136] and SiO_2.[137] The energetic positions of the CB and VB edges of selected semiconductors *vs.* some standard half-reaction potentials can be seen in Fig. 27. The heterojunction can significantly facilitate the separation of photogenerated carriers, hinder carrier recombination, and extend the absorption threshold into the visible light region, which can be ascribed to the effective matching of the energy band structure.[131] The two (or more) semiconductors of the heterojunction can form inherent electric fields, leading to a shift in individual Fermi level, and it finally settled at a uniform value.[51] According to the types of semiconductors, the heterojunctions can be divided into p–p, p–n and n–n heterojunctions. The Fermi levels for p-type and n-type semiconductors were close to the VB and CB, respectively. Hole transfer occurred in p–p heterojunctions; the hole depletion layer was generated on one side, and the hole accumulation layer was generated on the other side, until the Fermi energy levels were equal,[138] building an internal electric field. Due to different potentials, electron transfer proceeded until the Fermi energy level reached equilibrium,[139] and p–n heterojunctions can generate a built-in electric field, promoting charge separation (Fig. 28). After the Fermi energy level of an n–n semiconductor reached equilibrium through electron transfer, the Z-scheme mechanism would finally occur in photocatalysis.[140]

There have been many methods for heterojunction preparation, such as the *in situ* hydrothermal method,[141] *in situ* deposition,[142] co-precipitation,[143] *in situ* calcination,[144] chemical vapor deposition,[145] and ball milling.[146] The lattice parameters and tetragonal structures of SnO_2 were similar to those of TiO_2; photoinduced electrons can transfer from TiO_2 to the SnO_2 CB; holes can transfer in the reverse direction; the TiO_2/SnO_2 heterojunction promoted charge carrier separation and suppressed their recombination.[135] Because the band gap of SnO_2 was larger than that of TiO_2, the light absorption spectra of the SnO_2/TiO_2 heterojunction led to a blue shift compared with TiO_2. The improved photocatalytic activity for the SnO_2/TiO_2 heterojunction could be due to the coexistence of rutile and anatase phases, reduced band-gap energy, increased active sites, and suitable content of OH^- groups on the SnO_2/TiO_2 surface.[147] After selective oxidation of toluene to benzaldehyde by S-scheme TiO_2/Bi_2WO_6 under visible light irradiation, the composites exhibited excellent photocatalytic performance: the benzaldehyde production rate was 1725.41 μmol g^{-1} h^{-1}, 2.31 and 1.91 times higher than that of TiO_2 and Bi_2WO_6, respectively, where the excellent performance can be ascribed to the formation of a heterojunction by loading TiO_2 nanoparticles, improving the separation efficiency of photogenerated carriers.[148] For CdS–TiO_2, photogenerated electrons can transfer from the CdS CB to TiO_2 due to the less positive CB of CdS, while photogenerated holes of the TiO_2 VB can accumulate in the CdS VB and form a hole center, effectively reducing the charge carrier recombination rate, further improving the photocatalytic degradation efficiency for benzene.[133]

TiO_2 and NH_2-MIL-125 could be excited under UV light, and the photoinduced electrons migrated to the NH_2-MIL-125 VB through interactions between TiO_2 and NH_2-MIL-125; then the

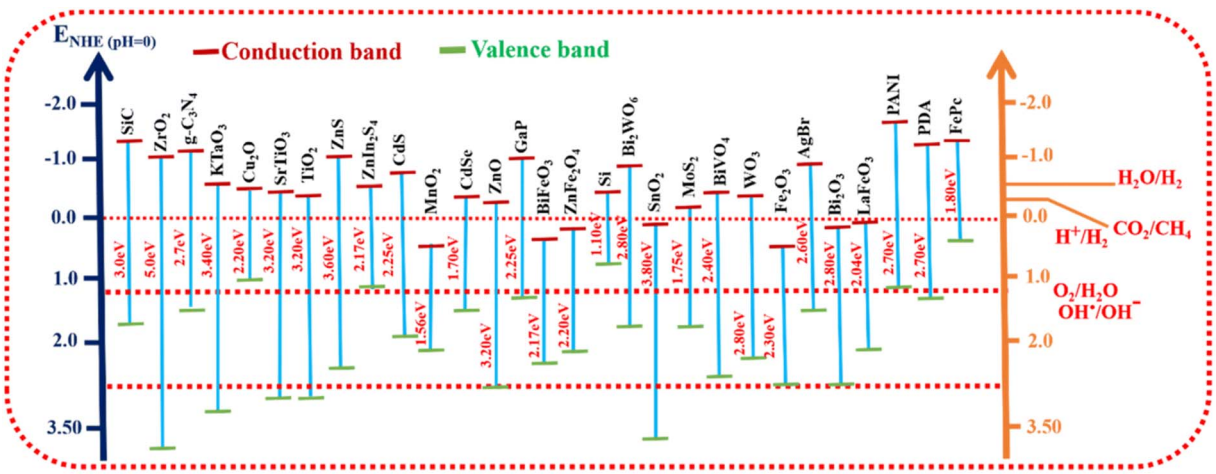

Fig. 27 Energy positions of the CB and VB edges of specific semiconductors *vs.* different standard half-reaction potentials.[131] Reprinted with permission from ref. 131 Copyright 2024, Royal Society of Chemistry.

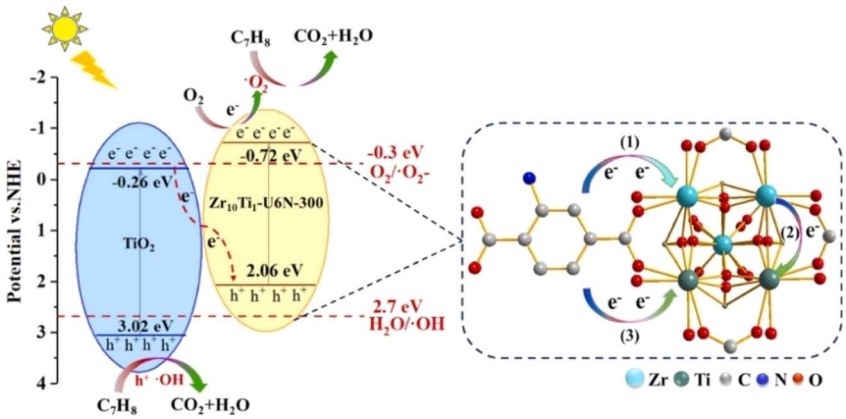

Fig. 28 Reaction mechanism for toluene photocatalytic oxidation over $Zr_{10}Ti_1$–U6N-300@TiO_2.[132] Reprinted with permission from ref. 132 Copyright 2025, Elsevier.

generated electrons migrated from the VB to the CB, while the holes remained at the TiO_2 VB, and the heterojunction interface provided an efficient electron transfer pathway.[149] The CB/VB of TiO_2 was −0.24/2.86 eV, while that for NH_2-MIL-125 was −0.72/1.75 eV, which, combined with the standard redox potentials of $OH^-/{}^{\bullet}OH$ (2.7 V *vs.* NHE) and $O_2/{}^{\bullet}O_2^-$ (−0.3 V *vs.* NHE) couples, meant that only holes from the TiO_2 VB could react with H_2O molecules to produce ${}^{\bullet}OH$.[149] While only electrons from the NH_2-MIL-125 CB could react with the adsorbed O_2 molecules to generate ${}^{\bullet}O_2^-$, HCHO was oxidized to H_2O and CO_2 by these ROSs.[149] However, there were several setbacks hindering the application of heterojunctions, such as different lattice structure constants or atomic thermal expansivity, which can lead to distortion of the interfacial lattice, where lattice distortion can promote the recombination of the charge carriers.[150]

5.6. Construction of a homojunction

Homojunction photocatalysts were prepared from materials with the same chemical composition but various band structures or crystal phases, where various band potential values of components formed a spatial charge layer at the homojunction interface.[150] Similar to heterojunctions, the construction of homojunctions can change the relative position of the energy band, the built-in electric field can transfer photogenerated carriers to the reverse direction, and the matching chemical and electronic structure of homojunctions are favorable for the separation and transfer of carriers (Fig. 29).[153] There was virtually no mismatch in homojunction lattices, and the same components on both sides of the homojunction interface could also avoid a discontinuity of band bonding.[150] Generally, homojunction photocatalysts are divided into two types: p–n junctions and n–n junctions. TiO_2-based homojunctions could be constructed in many different forms, like different dimensions (nanoparticles, nanobelts, nanosheets), crystal phases (anatase, rutile and brookite), crystal facets or morphologies, which can exhibit beneficial synergistic effects in the photocatalytic reaction.

TiO_2-based homojunctions were commonly constructed by merging TiO_2 with different crystal phases, and the electron bridge between different TiO_2 polymorphs can facilitate electron transfer;[155] therefore, the electrons generated on anatase CB jumped easily to less positive rutile, hindering the recombination of electrons and holes in anatase sites.[156] Fig. 30 shows the band gap energies of anatase, rutile, and brookite TiO_2, with mixed phases showing better photocatalytic activity than TiO_2 with a pure anatase phase. For mixed-phase TiO_2, the oxidation and reduction processes could be accelerated, because the oxidation process was limited in the anatase structure and the reduction process was limited in the rutile structure. The increased activity can be generally attributed to the interaction of the two forms, so this mixed phase with interfacial electron trapping sites can enhance the photocatalytic activity of TiO_2.[151]

Homojunctions with various dimensions, morphologies or facets, like quantum dots (0D)/nanosheets (2D), and nanobelts (1D)/nanosheets (2D), were prepared.[150] TiO_2 QDs were loaded onto the surface of TiO_2 nanoparticles; the electrons were redistributed at the interface of TiO_2 QDs and TiO_2 nanoparticles, which facilitated hole accumulation on the side of TiO_2 QDs, while electrons accumulated at TiO_2 nanoparticles, notably promoting charge separation and interfacial transfer; TiO_2 QDs and adjacent TiO_2 nanoparticles generated

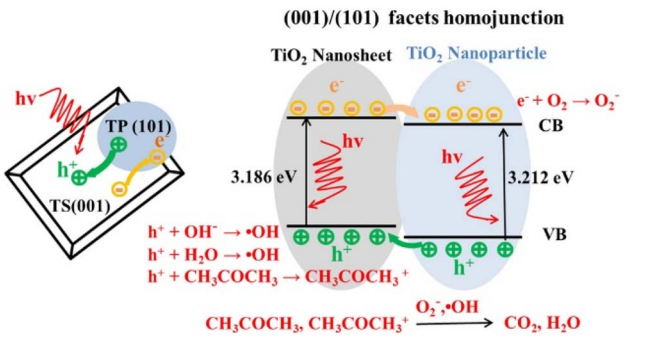

Fig. 29 Illustration of the synergetic effect of the homojunction of anatase TiO_2 nanoparticles (TP) with dominant (101) facets and nanosheets (TS) with dominant (001) facets.[153] Reprinted with permission from ref. 153 Copyright 2019, Elsevier.

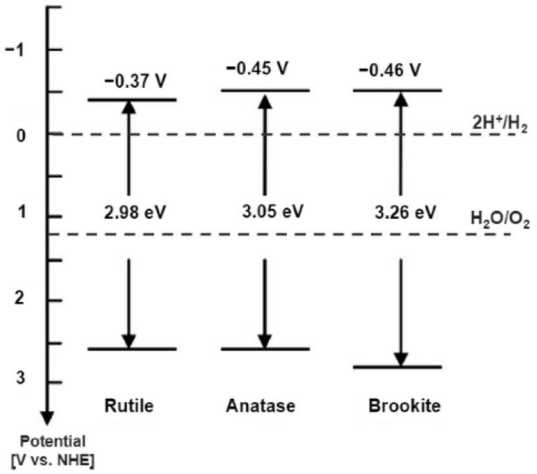

Fig. 30 Band-gap energies, VB, and CB for anatase, rutile, and brookite on the potential scale (V) *versus* the normal hydrogen electrode (NHE).[151] Reprinted with permission from ref. 151 Copyright 2023, MDPI.

a quantum-scale catalytic area, which significantly increased the toluene mineralization efficiency to 95.8% over QD-loaded TiO_2.[157] For a rutile TiO_2 nanorod@nanoparticle homojunction, the CB of the rutile TiO_2 nanoparticle could be elevated *via* a quantum effect, and absolute charge separation could be realized through long-distance transfer of electrons along the single-crystalline nanorod.[158] Moreover, nanoparticles embedded onto a nanorod roughened the smooth surface, promoting light absorption and generating more charge carriers. The nanorod@nanoparticle homojunction showed notably enhanced photocatalytic performance for benzene decomposition—the CO_2 yield was 10 times that of a nanorod array—where the enhanced photocatalytic activity could be attributed to higher photo-to-electron conversion efficiency and effective charge separation.[158] When microporous TiO_2 was loaded onto the surface of anatase TiO_2, the homojunction notably enhanced photogenerated carrier separation efficiency; it could also form microporous structures and an enlarged surface area, favorable for the concentration of toluene and intermediates near the photocatalytic sites; and the toluene mineralization efficiencies of the homojunction were 1.78 and 2.12 times higher than those of microporous TiO_2 and anatase TiO_2.[159]

The concept of a facet heterojunction was also proposed, indicating that the energy band structures and band edge locations were different for different facets (3.18 eV for the (001) facet, 3.22 eV for the (101) facet, and 3.23 eV for the (010) facet) (Fig. 31); therefore, different facets can be used to form surface heterojunctions.[117] The crystals with (001) and (010) facets exposed were favorable for a photo-oxidative reaction due to the high density of Ti_{5c} sites, and the crystals with (101) and (010) facets exposed were favorable for a photo-reductive reaction because of the higher energy of electrons at the CB minimum, as shown in Fig. 29 and 32. Anatase TiO_2 nanoparticles predominantly exposing (101) facets (TP) were loaded onto anatase TiO_2 nanosheets predominantly exposing (001) facets (TS) to form a TP/TS junction (Fig. 33).[153] TEM images of TP/TS

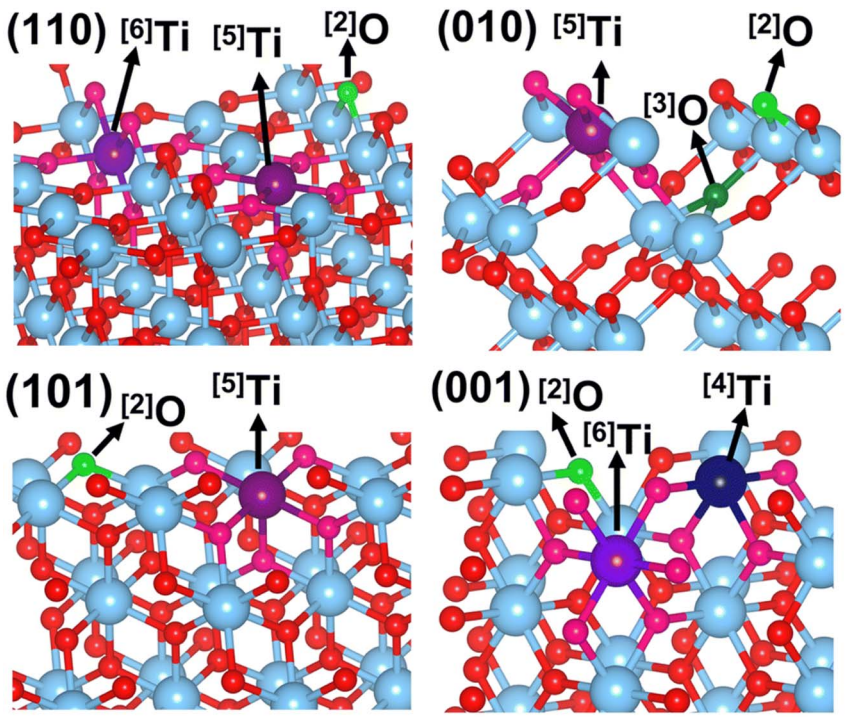

Fig. 31 Rutile (110), (010), (101), and (001) facets and surface atom coordination (bright green $^{[2]}O$, dark green $^{[3]}O$, and dark blue $^{[4]}Ti$, dark purple $^{[5]}Ti$, light purple $^{[6]}Ti$) on each. Red atoms are O and light blue are Ti.[152] Reprinted with permission from ref. 152 Copyright 2023, Royal Society of Chemistry.

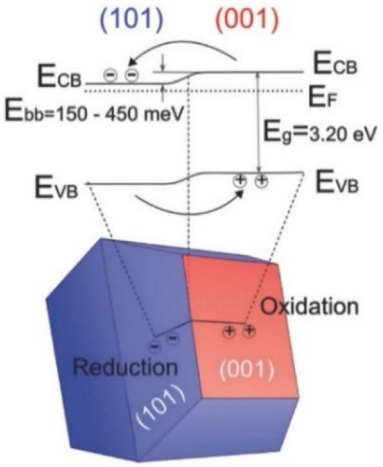

Fig. 32 Interfacial band bending and charge carrier spatial separation over anatase crystallites with both (001) and (101) facets exposed.[154] Reprinted with permission from ref. 154 Copyright 2018, John Wiley and Sons.

(2.5%), TP/TS (5%) and TP/TS (10%) can be seen in Fig. 33. For a TP/TS homojunction, holes in the VB of TiO_2 nanoparticles transferred to the VB of TiO_2 nanosheets, while electrons from the CB of TiO_2 nanosheets transferred to the CB of TiO_2 nanoparticles; during acetone degradation over optimized TP/TS (5%), CO_2 production rates were 5.4, 4.0 and 3.3 times higher than those over TP, TS and P25.[153]

6. Immobilization of photocatalysts

6.1. Immobilization method

For the practical application of photocatalysis for VOC degradation, the photocatalysts should be immobilized onto supports, and it was found that TiO_2 film showed higher catalytic activity than most TiO_2 powders. The main functions of loading photocatalysts onto supports were as follows: (1) enhancing dispersion and specific surface area; (2) facilitating photogenerated carrier separation; (3) strengthening light absorption capacity; (4) improving stability and recyclability; (5) simplifying recovery and practical application; (6) synergistic catalytic effect with photocatalysts. Various methods were applied for TiO_2 immobilization, like sol–gel, chemical/physical vapor deposition, electrophoretic deposition, and thermal spraying; then the photocatalyst layer was usually treated under high-temperature calcination to obtain TiO_2 with high crystallinity and be strongly adhered on supports.[167]

Immobilization methods can be divided into two types. The first was to treat photocatalyst powders *via* directly dip-coating or sintering (sometimes called wash-coating).[168] The other method was to load TiO_2 film onto the supports with various methods, like sol–gel, chemical vapor deposition (CVD), metal–organic CVD (MOCVD), and spray coating.[169] Thermal treatments were technically simple, but there was a significant barrier to practical preparation for scaled-up reactors, since they consumed abundant energy, which may increase the overall cost. The successful exploitation of a room-temperature

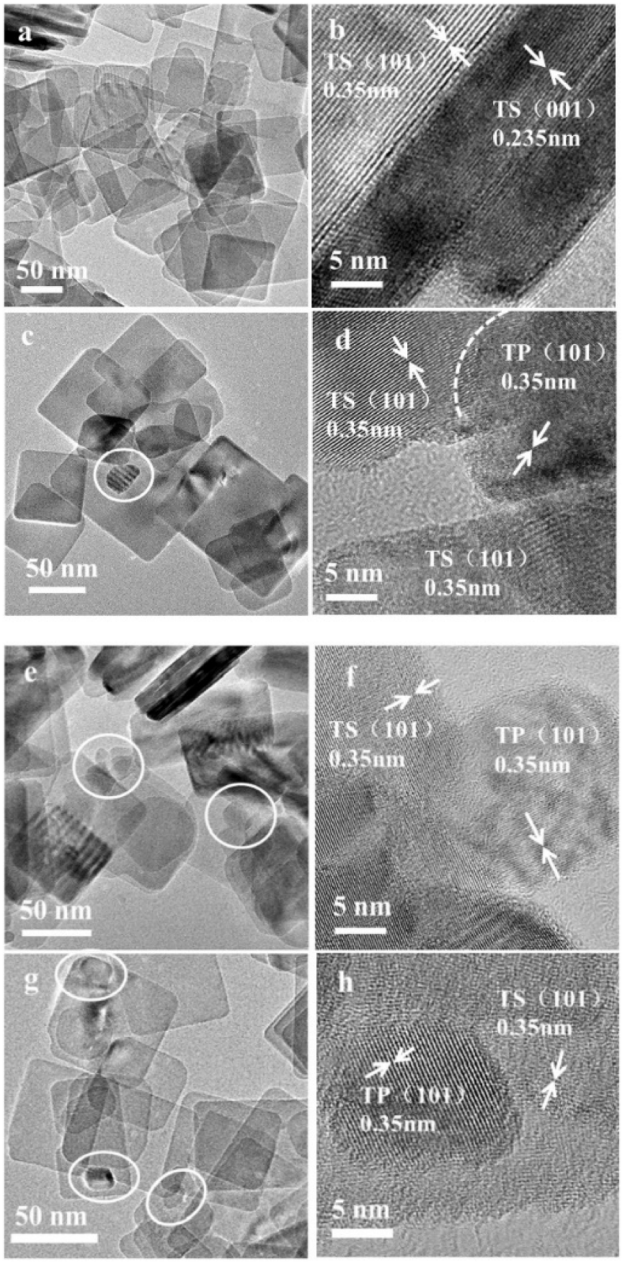

Fig. 33 TEM and HRTEM of TiO_2 homojunction with different ratios of TP/TS: TS (a and b), TP/TS (2.5%) (c and d), TP/TS (5%) (e and f), TP/TS (10%) (g and h).[153] Reprinted with permission from ref. 153 Copyright 2019, Elsevier.

immobilization method would be a breakthrough in promoting practical applications of photocatalysts.[167] A desirable immobilization method should possess the following characteristics: (1) durable and stable immobilization; (2) sufficient contact between photocatalyst and pollutant; (3) non-selectivity for various substrates; and (4) suitability and effectiveness for large-scale application.[63] Choosing an appropriate preparation and immobilization method to immobilize the photocatalyst is very important for improving photocatalytic efficiency.

Sol–gel was a wet-chemical method, where precursors were suspended in liquid phase, then put under gel conditions until

the photocatalyst film (sol–gel) became dehydrated.[35] Various methods have been used to load precursor solution on supports to form the photocatalyst film. Drying time was required to remove the solvent, and then the photocatalyst was substantially loaded on the support after densification and shrinkage, when thermal treatment was necessary to densify the photocatalyst layer. Vanadium and nitrogen co-doped TiO_2 was loaded on the honeycomb ceramics of continuous-flow photocatalytic degradation reactors, and the introduction of V/N dopants narrowed the band gap and widened the light absorption range of TiO_2, resulting in continuous and nearly-complete toluene photocatalytic degradation, where the degradation efficiency for toluene gas could reach 97.8%.[170]

The chemical vapor deposition technique was also used to prepare TiO_2 film. The precursors were transformed into vapor and injected into a chamber, where an anatase TiO_2 layer was loaded onto the substrate by the corresponding reaction, and they were used for the photocatalytic degradation of benzene.[171] TiO_2 thin films with specific crystal structure, high crystallinity, high porosity and high surface area can be obtained using this method. Physical vapor deposition was a simple and eco-friendly method to immobilize TiO_2 onto supports, because it required no harsh chemicals or residual solvents. Molecules from a target material were ejected onto substrates to form TiO_2 thin film, and films prepared by physical vapor deposition exhibited improved photocatalytic activity compared to conventional TiO_2 films.[172]

Electrochemical deposition was a feasible method, in which the main ions in an electrolyte could participate in an electrochemical reaction under particular conditions to load target products onto the gap of a photonic crystal which was used as an electrode.[173] The gap of the template could be filled with parent material, and the exact reverse replica could be easily obtained from the original opal template.[173] Electrochemical deposition was also used for coating a photocatalyst, where a three-dimensional polymer, SU8, was used as a template, and a sol–gel of TiO_2 fully filled the polymer template through electrochemical deposition, so a photonic crystal with reversed structure could be obtained.[174] Electrophoresis was a suitable method for covering a variety of materials on electrically conductive surfaces with two electrodes, where the powder was used as the solvent solution for depositing photocatalysts. Additives (like acetylacetone and isopropanol) were usually applied to improve the conductivity of the suspension, which could make the consequent coating more uniform and stable.

Spray-coating and dip-coating were simple and low-cost methods used for coating photocatalysts. Initially, photocatalysts were dispersed in a suitable solvent, such as methanol or ethanol, which were then sprayed on the substrate, and the photocatalysts were immobilized onto the substrate after solvent evaporation. Aerosol-assisted technologies, like spray atomization (SA), spray gun (SG) and spray-drying (SD), were applied for TiO_2 deposition onto fibrous filter media. A TiO_2 layer deposited by SG and SA methods showed excellent photocatalytic performance for the degradation of toluene, while a TiO_2 layer deposited by SD showed poor photocatalytic performance and stability.[175] TiO_2 was dispersed in ethanol solvent to form a slurry, and then sprayed onto a glass plate by an aero spray, and TiO_2 immobilization could be achieved after drying at room temperature.[45] In some research, additional chemical binders were also used to strongly and uniformly immobilize the photocatalysts onto the substrate.[46] However, the photocatalytic activity may decrease because of the reduced available surface area caused by chemical binders. Thermal spraying can quickly immobilize photocatalysts onto substrates, but a higher temperature used for spraying may change the photocatalyst crystal structure and finally decrease its photocatalytic activity.

Interfacial polymerization was also used for immobilizing photocatalysts onto the substrate. The interfacial polymerization reaction was usually carried out between two different monomers (water hating and water loving) at the oil–water interface. Nylon/TiO_2 was immobilized onto polysiloxane-coated paper *via* interfacial polymerization.[166] Tetraethyl orthosilicate and 3-aminopropyltrimethoxysilane (as silane coupling agent) were used to synthesize polysiloxane-coated paper, and cationic TiO_2 was combined with anionic polysiloxane-coated paper *via* electrostatic interactions. The paper showed excellent degradation performance for acetaldehyde, and the structure of photocatalyst layer remained unchanged for 240 h under UV light illumination.[166]

6.2. Substrate type

The type of substrate influenced PCO performance, where the low adsorption capacity of TiO_2 could be improved by constructing composites with substrates, and VOCs could be adsorbed on the substrates, forming a high-concentration environment of VOCs around the loaded TiO_2, enhancing the photocatalytic reaction rate.[171] The physical and chemical characteristics of the substrates should be stable in photochemical oxidation reactions, and the surface area of the substrates should be high enough to load photocatalysts. Other essential characteristics of the substrates were sufficient adhesion to TiO_2 particles, strong adsorbability with VOCs, and resistance to sintering temperature. Various materials, like activated carbon fibers,[177] carbon nanotubes,[178] glass,[84] glass fibers,[179] fiberglass fibers,[180] polymeric materials,[168] zeolites,[176] and stainless steel,[181] have been used as substrates (Table 1).

Activated carbon with high porosity can create a high specific surface area and improve the photocatalytic activity of hybrid photocatalysts. Carbonized cotton fibers (CCFs) showed great resistance to corrosion and temperature, and the conductivity and strength of CCFs were high enough for photocatalysis, so they were alternative supports for TiO_2.[177] When nanostructured TiO_2 was immobilized on ACFFs, TiO_2/ACFF was used for toluene degradation, and the removal efficiency increased from 41% (for TiO_2 power) to 97% (for TiO_2/ACFF), which could be ascribed to hindered electron–hole pair recombination and reduced band-gap energy by ACFF.[182]

Glass and silica substrates were transparent, and were widely used for the immobilization of photocatalysts. Furthermore, glass fibers were simpler to treat than other supports due to their high flexibility; when Fe-doped TiO_2 was immobilized on

Table 1 Different deposition methods and types of support for photocatalyst preparation

VOCs	Immobilization method	Features	Photocatalyst/support	Removal efficiency	Reference
Benzene	Dip coating	The loading amount can be flexibly controlled to promote interface contact and retain carrier structure, but the active component was unevenly distributed, and the loading amount was limited	g-C_3N_5-coupled TiO_2/ceramic balls	93.9% (1 ppm, UV light, 20 min)	160
Toluene	Physical coating	Retaining the intrinsic properties of the material, flexible and controllable, low cost, but poor stability, and uneven contact	Anatase and bronze phase TiO_2/stainless steel disk	97% (100 ppm, UV light, 60 min)	161
Acetaldehyde	Drop casting	Little interference with material properties, controllable load and thickness, strong substrate compatibility, but weak binding force and poor uniformity	Mesoporous TiO_2/dry glass slides	82% (77 ppm, UV light, 250 mL min^{-1})	162
Toluene	Step-by-step electrospinning–spraying	The multi-level structure optimizes mass transfer and light utilization, flexible regulation of load, balance of activity and stability, but a risk of interface bonding and high cost	TiO_2/non-woven fabrics	93% (78 ppm, UV light, 240 min)	163
HCHO	Pulp coating	Intrinsic properties of the catalyst were retained, the load was flexibly controlled, substrate compatibility was strong, but the binding force was weak, so it easily fell off, and the distribution uniformity was poor	Na/@TiO_2(B)-O_v/filter membrane	80% (65 ppm, visible light, 100 mL min^{-1})	164
m-Xylene	Solvent deposition	Simple operation, needs no thermal treatment, can form on any complex substrate, but high cost of the precursor and not suitable for large-scale preparation	TiO_2/glass plate	~96.0% (1000 ppm, UV light, cyclic 200 mL min^{-1})	165
Acetaldehyde	Interfacial polymerization	No usage of binding agent, regulated interface structure, stable structure, but high cost	TiO_2/nylon film	~100% (250 ppm, UV light, 240 min)	166

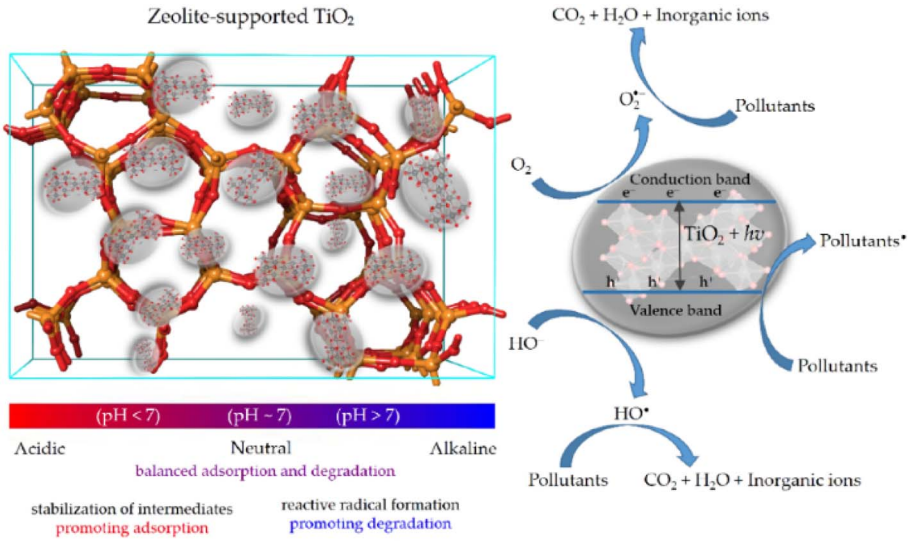

Fig. 34 Schematic illustration of photocatalysis mechanism for TiO_2–zeolite composite.[176] Reprinted with permission from ref. 176 Copyright 2025, MDPI.

glass fiber, it showed excellent VOC photocatalytic removal efficiency under both UV light and visible light irradiation.[179] TiO_2 was immobilized on fiberglass fibers (FGFs), TiO_2/FGFs showed hydrophilic characteristics and higher adsorption ability for polar VOCs than for non-polar VOCs under the same RH levels, which enhanced photocatalytic oxidation efficiency for VOCs.[180] TiO_2 was immobilized onto porous polyurethane and used for the photocatalytic removal of toluene with visible light, where immobilization improved both the photocatalytic oxidation and adsorption performance of TiO_2.[170]

Zeolites with high surface area, a crystalline framework, and well-defined pore structure showed selective adsorption of organic and inorganic pollutants, which could effectively concentrate them near photocatalytic sites of TiO_2, and the reaction efficiency was significantly increased *via* a "pre-concentration effect", where the pollutants were more easily available for photocatalytic degradation, and zeolite-supported TiO_2 composites promoted the formation of ROS, such as $^{\bullet}OH$, which were crucial for the degradation of organic pollutants (Fig. 34).[176] Functional substrates were also used for immobilizing photocatalysts, such as metal–organic frameworks (MOFs), where MOF substrates could work as photosensitizers to realize efficient light harvesting and provide more active sites for photocatalysis, thus improving VOC photodegradation.[132]

7. Summary and perspectives

TiO_2-based photocatalytic oxidation technology is promising for the purification of indoor VOCs, which could effectively degrade VOCs to CO_2 and H_2O at room temperature, and the development of a high-efficiency photocatalyst is crucial for this technology. However, limitations, like fast recombination of charge carriers, low quantum efficiency, poor visible light photocatalytic activity, and catalyst deactivation, have limited their practical application. This review has thoroughly summarized the methods for improving the photocatalytic purification of indoor VOCs from the perspective of TiO_2 modification, based on some intrinsic characteristics of VOCs, such as metal and non-metal doping, coupling of different semiconductors, surface/interface design, and TiO_2 immobilization.

Future trends in PCO purification for indoor VOCs include the development of highly stable and efficient photocatalysts, hydrophobic photocatalysts to hinder the negative effects of water vapor on PCO, novel PCO reactors with a UV-LED source, hybrid technologies (such as photothermal and photoelectric catalysis), catalysts and equipment for VOC degradation in scale-up. Furthermore, under actual conditions, such as a mixture of VOCs, sub-ppm levels of VOCs and high moisture content, the performance and economy of the novel air purification units should also be critically evaluated. This review could offer guidance for the development of TiO_2-based photocatalysts for the efficient purification of indoor VOCs.

Author contributions

Lian Yu: investigation, methodology, formal analysis, supervision, writing – review & editing. Yajing Duan: writing – review & editing. Dabin Wang: investigation, methodology, formal analysis, validation, review & editing. Zhen Liang: formal analysis, writing – review & editing. Cunzhen Liang: project administration, resources, supervision, visualization. Yafei Wang: project administration, resources, validation, visualization.

Conflicts of interest

The authors declare that they have no known competing financial interests or personal relationships that could have appeared to influence the work reported in this paper.

Data availability

There is no additional data associated with this article.

Acknowledgements

This work was supported by the National Nature Science Foundation of China (Grant No. 52370108), the Third Xinjiang Scientific Expedition Program (Grant No. 2021xjkk1400), the National College Students Innovation and Entrepreneurship Training Program (Grant No. 2025J00015 and 2025J00016), the Zhiyuan Science Foundation of BIPT (Project No. 2023004).

References

1 P. Kumar, A. B. Singh, T. Arora, S. Singh and R. Singh, *Sci. Total Environ.*, 2023, **872**, 162163.
2 H. M. Wang, J. Y. Xiong and W. J. Wei, *Environ. Int.*, 2022, **168**, 107451.
3 V. Kaunelienė, M. Meišutovič-Akhtarieva and D. Martuzevičius, *Chemosphere*, 2018, **206**, 5688–578.
4 J. Kwak, B. A. Geier, M. M. Fan, S. A. Gogate, S. A. Rinehardt, B. S. Watts, C. C. Grigsby and D. K. Ott, *J. Sep. Sci.*, 2015, **38**(14), 2463–2469.
5 K. Bralewska, W. Rogula-Kozłowska and A. Bralewski, *Build. Environ.*, 2022, **208**, 108589.
6 X. N. Ren, F. W. Wang, X. C. Wang, M. L. Chen, W. K. Fang, X. Deng, P. L. Lu, Z. L. Li, H. Guo and N. L. Rose, *Atmos. Environ.*, 2025, **317**, 107979.
7 X. J. Zhou, J. L. Liu, X. J. Dong, R. X. Ma, X. K. Wang and F. H. Wang, *Sci. Total Environ.*, 2023, **864**, 161189.
8 Y. Cai, J. W. He, X. Y. Huang and F. Y. Zhao, *Indoor Built Environ.*, 2023, **32**(7), 1296–1318.
9 H. Qiu, C. H. Bai, K. J. Chuang, Y. C. Fan, T. P. Chang, S. H. L. Yim and K. F. Ho, *Chemosphere*, 2021, **276**, 130172.
10 X. T. Mu, H. L. Ding, W. G. Pan, Q. Zhou, W. Du, K. N. Qiu, J. C. Ma and K. Zhang, *J. Environ. Chem. Eng.*, 2021, **9**(4), 105650.
11 C. Protano, G. Buomprisco, V. Cammalleri, R. N. Pocino, D. Marotta, S. Simonazzi, F. Cardoni, M. Petyx, S. Iavicoli and M. Vitali, *Cancers*, 2022, **14**(1), 165.
12 C. H. Halios, C. Landeg-Cox, S. D. Lowther, A. Middleton, T. Marczylo and S. Dimitroulopoulou, *Sci. Total Environ.*, 2022, **839**, 156201.
13 V. Pertegal, E. Riquelme, J. Lozano-Serra, P. Cañizares, M. A. Rodrigo, C. Sáez and E. Lacasa, *J. Environ. Manage.*, 2023, **345**, 118798.
14 W. Q. Huang, Y. N. Li, X. F. Li, Z. Q. Zhang, Y. H. Lu, M. G. Peng, X. Y. Wang and Y. K. Zhou, *Sep. Purif. Technol.*, 2025, **363**, 132203.
15 P. Liu, H. M. Mathisen, M. Skaten and M. J. Alonso, *Build. Environ.*, 2022, **222**, 109430.
16 D. G. Lai, Z. Huang, Y. Y. Liu, B. Y. Chen and J. M. Hong, *Environ. Res.*, 2025, **270**, 120989.
17 Y. M. Zhang, F. F. Ge, Z. F. Hao, H. Y. Zhang and Y. F. Zhang, *Appl. Clay Sci.*, 2025, **270**, 107744.
18 H. B. Wu, Y. L. Li, J. Ji, N. S. Li and B. D. Yu, *Build. Environ.*, 2025, **268**, 112334.
19 X. Y. Gao, Y. Y. Deng, Z. N. Wei, Z. B. Li, N. Z. Peng, X. Y. Li, L. Li, L. C. Jiang, S. X. Qiu, D. H. Zhao and S. Kawi, *J. Environ. Chem. Eng.*, 2025, **13**(2), 116045.
20 T. H. Zhang, R. Miao, J. R. Ding, Y. Gao and Y. D. Rao, *Indoor Built Environ.*, 2025, **34**(3), 644–660.
21 M. I. Severino, A. A. Mohtar, C. V. Soares, C. Freitas, N. Sadovnik, S. Nandi, G. Mouchaham, V. Pimenta, F. Nouar, M. Daturi, G. Maurin, M. L. Pinto and C. Serre, *Angew. Chem., Int. Ed.*, 2023, **62**(6), e202211583.
22 Y. G. Zhang, Y. F. Wang, R. J. Xie, H. B. Huang, M. K. H. Leung, J. T. Li and D. Y. C. Leung, *Environ. Sci. Technol.*, 2022, **56**(23), 16582–16601.
23 E. Greco, A. D. Spirt, A. Miani, P. Piscitelli, R. Trombin, P. Barbieri and E. Marin, *Appl. Sci.*, 2025, **15**(3), 1629.
24 A. Fujishima and K. Honda, *Nature*, 1972, **238**, 37–38.
25 S. Almaie, V. Vatanpour, M. H. Rasoulifard and I. Koyuncu, *Chemosphere*, 2022, **306**, 135655.
26 Y. C. Zhang, Y. J. Zhou, X. Y. Dong, X. G. Xi and P. Y. Dong, *Chem. Eng. J.*, 2024, **496**, 154186.
27 P. Haghighi and F. Haghighat, *Build. Environ.*, 2024, **249**, 111108.
28 N. Li, W. Zhang, D. L. Wang, G. X. Li and Y. Zhao, *Chem.–Asian J.*, 2022, **17**(23), e202200822.
29 Y. X. Wang, Y. Y. Zhang, X. J. Zhu, Y. Liu and Z. B. Wu, *Appl. Catal., B*, 2022, **316**, 121610.
30 L. Ma, C. F. Huang, X. C. Li, X. An, J. P. Li, L. Zou, X. X. Zhu, C. Yuan, X. Dai, Y. W. Zhou, X. Zhu and C. C. Tian, *Sep. Purif. Technol.*, 2025, **354**, 128635.
31 H. Khan and M. U. H. Shah, *J. Environ. Chem. Eng.*, 2023, **11**(6), 111532.
32 D. Kotzias, *Crystals*, 2024, **14**(7), 661.
33 Y. C. Wei, H. Meng, Q. Wu, X. Y. Bai and Y. Q. Zhang, *Catalysts*, 2023, **13**, 1466.
34 E. P. E. Ruiz, J. L. Lago and S. P. Thirumuruganandham, *Materials*, 2023, **16**(8), 3076.
35 Y. Ahmadi and K. H. Kim, *Renewable Sustainable Energy Rev.*, 2024, **189**, 113948.
36 R. Cheng, M. Zhang, P. P. Zhou, N. Ye and P. Yang, *Surf. Interfaces*, 2025, **62**, 106205.
37 D. F. Jiang, T. A. Otitoju, Y. Y. Ouyang, N. F. Shoparwe, S. Wang, A. L. Zhang and S. X. Li, *Catalysts*, 2021, **11**(9), 1039.
38 S. C. Lv, M. X. Pei, Y. X. Liu, Z. C. Si, X. D. Wu, R. Ran, D. Weng and F. Y. Kang, *Nano Res.*, 2022, **15**(7), 5848–5856.
39 A. Kumar, P. Choudhary, A. Kumar, P. H. C. Camargo and V. Krishnan, *Small*, 2022, **18**(1), 2101638.
40 Y. Yang, H. Luo, R. Liu, G. Li, Y. Yu and T. An, *Ecotoxicol. Environ. Saf.*, 2020, **197**, 110615.
41 C. Wu, Q. L. Liu, Y. Zhan, W. Tan, X. Q. Wei, Q. Tong, H. Q. Wan and L. Dong, *Chem. Eng. J.*, 2023, **475**(1), 146294.
42 Q. Q. Wu, J. N. Ye, W. Qiao, Y. W. Li, J. W. (Hans) Niemantsverdriet, E. Richards, F. Pan and R. Su, *Appl. Catal., B*, 2021, **291**, 120118.
43 X. B. Zhu, C. Jin, X. S. Li, J. L. Liu, Z. G. Sun, C. Shi, X. G. Li and A. M. Zhu, *ACS Catal.*, 2017, **7**(10), 6514–6524.

44 C. Mao, H. R. Ling, L. Yi, R. S. Zhu and G. Zhang, *Chem. Eng. J.*, 2023, **473**, 145366.
45 M. Kask, J. Bolobajev and M. Krichevskaya, *Chem. Eng. J.*, 2020, **399**, 125815.
46 V. T. T. Ho, D. H. Chau, K. Q. Bui, N. T. T. Nguyen, T. K. N. Tran, L. G. Bach and S. N. Truong, *Inorganics*, 2022, **10**(3), 29.
47 D. Selishchev, D. Svintsitskiy, L. Kovtunova, E. Gerasimov, A. Gladky and D. Kozlov, *Colloids Surf., A*, 2021, **612**, 125959.
48 J. F. Chen, L. Chen, X. Wang, Z. P. Rao, J. Sun, A. Y. Chen and X. F. Xie, *J. Colloid Interface Sci.*, 2022, **605**, 674–684.
49 T. Mao, J. Y. Zha, Y. Hu, Q. Chen, J. M. Zhang and X. K. Luo, *Inorganics*, 2024, **12**(7), 178.
50 J. C. Liang, J. Y. Wang, K. X. Song, X. F. Wang, K. F. Yu and C. Liang, *J. Rare Earths*, 2020, **38**(2), 148–156.
51 Y. Q. Si, M. Mamatrishat, B. Yiliyasi and X. Fuerkaiti, *Phys. Lett. A*, 2024, **525**, 129929.
52 Y. Sari, P. L. Gareso and D. Tahir, *Int. J. Environ. Sci. Technol.*, 2025, **22**(1), 1975–1994.
53 J. F. Chen, L. Chen, X. Wang, J. Sun, A. Y. Chen and X. F. Xie, *Appl. Surf. Sci.*, 2022, **596**, 153655.
54 D. Jang, Y. Kim, J. Lee, H. Shin and M. Kang, *Surf. Interfaces*, 2024, **55**, 105394.
55 Z. Shayegan, F. Haghighat and C. S. Lee, *J. Cleaner Prod.*, 2021, **287**, 125462.
56 M. Chen, H. H. Wang, X. Y. Chen, F. Wang, X. X. Qin, C. B. Zhang and H. He, *Chem. Eng. J.*, 2020, **390**, 124481.
57 L. Rossi, M. Palacio, P. I. Villabrille and J. A. Rosso, *Environ. Sci. Pollut. Res.*, 2021, **28**(19), 24112–24123.
58 A. Mantilla, E. S. Benitez, I. M. Valenzuela, G. R. Ortiz, S. C. Díaz, L. L. Rojas, F. J. T. Morales and M. N. Magaña, *J. Photochem. Photobiol., A*, 2025, **459**, 116079.
59 H. H. Fan, J. Y. Su, E. Zhao, Y. M. Zheng and Z. P. Chen, *J. Colloid Interface Sci.*, 2025, **684**, 140–147.
60 S. Ahmetović, Z. Ž. Vasiljević, J. B. Krstić, M. Finšgar, D. Solonenko, D. Bartolić, N. B. Tadić, G. Miskovic, N. Cvijetićanin and M. V. Nikolic, *Surf. Interfaces*, 2024, **49**, 104434.
61 L. Díaz, V. D. Rodríguez, M. González-Rodríguez, E. Rodríguez-Castellón, M. Algarra, P. Núñez and E. Moretti, *Inorg. Chem. Front.*, 2021, **8**(14), 3491–3500.
62 Z. Shayegan, C. S. Lee and F. Haghighat, *Chem. Eng. J.*, 2018, **334**, 2408–2439.
63 F. T. Geldasa, F. B. Dejene, M. A. Kebede, F. G. Hone and E. T. Jira, *Sci. Rep.*, 2025, **15**(1), 3390.
64 S. B. Patil, P. S. Basavarajappa, N. Ganganagappa, M. S. Jyothi, A. V. Raghu and K. R. Reddy, *Int. J. Hydrogen Energy*, 2019, **44**(26), 13022–13039.
65 A. Jaison, A. Mohan and Y. C. Lee, *Catalysts*, 2023, **13**(2), 407.
66 A. Kubiak, A. Grzegórska, E. Gabała, J. Zembrzuska, M. Szybowicz, H. Fuks, A. Szymczyk, A. Zielińska-Jurek, M. Sikorski and T. Jesionowski, *J. Photochem. Photobiol., A*, 2023, **437**, 114428.
67 L. Jiang, Z. F. Luo, Y. Z. Li, W. Wang, J. J. Li, J. Li, Y. L. Ao, J. He, V. K. Sharma and J. Q. Wang, *Chem. Eng. J.*, 2020, **402**, 125549.
68 B. Li, H. S. Zheng, T. Zhou, B. Y. Zi, Q. J. Lu, D. Q. Li, M. Zhang, Z. S. Qiu, Z. G. Luo, Y. M. Zhang, B. Xiao, M. P. Chen, J. Zhang, H. C. Sun, J. H. Zhao, T. W. He, Z. Q. Zhu, G. L. Zhang, Y. X. Zhang and Q. J. Liu, *Chem. Eng. J.*, 2024, **497**, 154726.
69 S. Y. Yuan, M. Chen, X. X. Qin, X. Y. Chen, J. H. Zhang and C. B. Zhang, *J. Environ. Sci.*, 2025, **147**, 561–570.
70 A. Piątkowska, M. Janus, K. Szymański and S. Mozia, *Catalysts*, 2021, **11**(1), 144.
71 A. K. Chakraborty, S. Ganguli and M. A. Sabur, *J. Water Process Eng.*, 2023, **55**, 104183.
72 J. Huang, L. Dou, J. Z. Li, J. B. Zhong, M. J. Li and T. Wang, *J. Hazard. Mater.*, 2021, **403**, 123857.
73 N. Kaur, S. K. Shahi, J. S. Shahi, S. Sandhu, R. Sharma and V. Singh, *Vacuum*, 2020, **178**, 109429.
74 V. Vallejo-Otero, N. Crespo-Monteiro, E. Gamet, N. Ollier, C. Donnet, A. Valour and Y. Jourlin, *J. Eur. Ceram. Soc.*, 2025, **45**(10), 117330.
75 D. H. Lim, H. A. Maitlo, S. A. Younis and K. H. Kim, *Mater. Today Nano*, 2024, **27**, 100499.
76 G. H. Lu, X. Wang, Y. Wang, G. S. Shi, X. F. Xie and J. Sun, *Chem. Eng. J.*, 2021, **408**, 127257.
77 S. Meng, Y. Zhuang, X. Yang, D. X. Guo and J. L. Li, *New J. Chem.*, 2025, **49**(9), 3526–3535.
78 M. Kamaei, H. Rashedi, S. M. M. Dastghei and S. Tasharrofi, *Catalysts*, 2018, **8**(10), 466.
79 Y. Sun, Y. Ahmadi and K. H. Kim, *Environ. Res.*, 2024, **260**, 119664.
80 L. R. Yang, X. Y. Liu, C. M. Wang, Z. G. Liu and X. X. Feng, *Opt. Mater.*, 2022, **133**, 112997.
81 L. T. Pérez-Poyatos, L. M. Pastrana-Martínez, S. Morales-Torres and F. J. Maldonado-Hódar, *Chem. Eng. J.*, 2025, **508**, 160986.
82 H. Heffner, R. Faccio and I. López-Corral, *Appl. Surf. Sci.*, 2021, **551**, 149479.
83 T. Kalampaliki, S. P. Makri, E. Papadaki, A. Grigoropoulos, A. Z. Karathanasis and I. Deligkiozi, *Nanomaterials*, 2021, **11**(10), 2543.
84 A. V. Vorontsov and H. Valdés, *Int. J. Hydrogen Energy*, 2019, **44**(33), 17963–17973.
85 T. Boningaria, S. N. R. Inturia, M. Suidanb and P. G. Smirniotis, *Chem. Eng. J.*, 2018, **339**, 249–258.
86 T. Kalampaliki, S. P. Makri, E. Papadaki, A. Grigoropoulos, A. Z. Karathanasis and I. Deligkiozi, *Nanomaterials*, 2021, **11**, 2543.
87 T. D. Pham and B. K. Lee, *Chem. Eng. J.*, 2017, **307**, 63–73.
88 K. Madan, S. Guru, M. Madan, R. Shanmugam, H. S. Rao and G. R. Rao, *J. Photochem. Photobiol., A*, 2024, **456**, 115816.
89 X. W. An, Y. J. Hou, W. J. An, J. S. Hu, H. Wang and W. Q. Cui, *Surf. Interfaces*, 2024, **55**, 105365.
90 J. J. Li, S. C. Cai, Z. Xu, X. Chen, J. Chen, H. P. Jia and J. Chen, *J. Hazard. Mater.*, 2017, **325**, 261–270.
91 D. Cherni, N. Moussa, M. F. Nsib, A. Olivo, M. Signoretto, L. Prati and A. Villa, *J. Mater. Sci.: Mater. Electron.*, 2019, **30**(20), 18919–18926.
92 X. T. Wu, Y. Su, Y. X. Wang, K. Amina, P. F. Zhu, P. Wang and G. D. Wei, *J. Colloid Interface Sci.*, 2024, **658**, 247–257.

93 X. Yan, Z. P. Xing, Y. Cao, M. Q. Hu, Z. Z. Li, X. Y. Wu, Q. Zhu, S. L. Yang and W. Zhou, *Appl. Catal., B*, 2017, **219**, 572–579.
94 S. R. Gu, M. Khan, Z. Yi and B. Wu, *Materials*, 2018, **11**(2), 313.
95 S. Khursheed, R. Tehreem, M. Awais, D. Hussain, M. I. Malik, Y. S. Mok and G. U. Siddiqui, *Nanomaterials*, 2022, **12**(13), 2246.
96 S. Sharma, R. Kumar, P. Raizada, T. Ahamad, S. M. Alshehri, V. H. Nguyen, S. Thakur, C. C. Nguyen, S. Y. Kim, Q. V. Le and P. Singh, *Environ. Res.*, 2022, **214**, 113995.
97 S. Douven, J. G. Mahy, C. Wolfs, C. Reyserhove, D. Poelman, F. Devred, E. M. Gaigneaux and S. D. Lambert, *Catalysts*, 2020, **10**(5), 547.
98 G. Jalloul, I. Keniar, A. Tehrani and C. Boyadjian, *Front. Environ. Sci.*, 2021, **9**, 1–29.
99 Z. Y. Zhong, Z. Z. Shen, Y. P. Zhang, J. Li and J. Z. Lyu, *Appl. Surf. Sci.*, 2023, **628**, 157306.
100 R. Ravi and A. K. Golder, *J. Environ. Chem. Eng.*, 2025, **13**(3), 116198.
101 S. Y. Zhong, D. X. Yu, Y. H. Ma, Y. H. Lin, X. Y. Wang, Z. Z. Yu, M. R. Huang, Y. D. Hou, M. Anpo, J. C. Yu, J. S. Zhang and X. C. Wang, *Angew. Chem., Int. Ed.*, 2025, e202502823.
102 W. Zhou and H. G. Fu, *Inorg. Chem. Front.*, 2018, **5**(6), 1240–1254.
103 W. B. Jiang, H. Y. Loh, B. Q. L. Low, H. J. Zhu, J. X. Low, J. Z. X. Heng, K. Y. T. Tang, Z. B. Li, X. J. Loh, E. Y. Ye and Y. J. Xiong, *Appl. Catal., B*, 2023, **321**, 122079.
104 S. C. Sharma, S. Torabnia, R. B. Harikrishna, H. S. Rao, A. V. Gopinathan, K. Hsu, G. R. Rao and A. M. Kannan, *Appl. Surf. Sci.*, 2025, **695**, 162900.
105 Q. J. Zhang, C. Yao, F. Zhang, Y. C. Chen, Z. L. Li, Y. K. Zhou, Y. X. Qin, L. Y. Xu, F. Feng, J. Zhao, C. S. Lu, Q. F. Zhang, Q. T. Wang and X. N. Li, *J. Mater. Chem. A*, 2025, **13**(7), 5180–5190.
106 W. Hiramatsu, Y. Shiraishi, S. Ichikawa, S. Tanaka, Y. Kawada, C. Hiraiwa and T. Hirai, *J. Am. Chem. Soc.*, 2025, **147**(2), 1968–1979.
107 X. H. Yu, J. G. Deng, Y. X. Liu, L. Jing, R. Y. Gao, Z. Q. Hou, Z. X. Zhang and H. X. Dai, *Environ. Sci. Technol.*, 2022, **56**(16), 11739–11749.
108 M. H. Chen, W. Z. Wang, Y. P. Qiu, H. Wen, G. Y. Li, Z. Q. Yang and P. Wang, *ACS Catal.*, 2022, **12**(9), 5565–5573.
109 S. D. Sun, X. M. Wu, Z. W. Huang, H. Z. Shen, H. W. Zhao and G. H. Jing, *Chem. Eng. J.*, 2022, **435**, 135035.
110 H. Dong, Y. K. Ji, Q. Shao, X. Y. Hu, J. Zhang, X. H. Yao and C. Long, *Sci. Total Environ.*, 2024, **924**, 171521.
111 L. L. Zhang, W. B. Chu, Q. J. Zheng and J. Zhao, *Phys. Chem. Chem. Phys.*, 2022, **24**(8), 4743–4750.
112 X. W. Sun, Z. D. Feng, S. Y. Wang, Q. N. Wang, P. F. Zhang, R. G. Li and C. Li, *ACS Catal.*, 2024, **14**(7), 5356–5365.
113 T. Wei, B. L. Niu and G. H. Zhao, *ACS Appl. Mater. Interfaces*, 2020, **12**(35), 39273–39281.
114 C. F. Zhao, L. Ren, Y. Shi, X. L. Wang, W. C. Huang and H. Xie, *J. Environ. Chem. Eng.*, 2025, **13**(2), 115764.
115 H. G. Yang, C. H. Sun, S. Z. Qiao, J. Zou, G. Liu, S. C. Smith, H. M. Cheng and G. Q. Lu, *Nature*, 2008, **453**(7195), 638–641.
116 B. Y. Li, J. Q. Chen, J. Li, Z. X. Jiang, Y. W. Hu, X. L. Wang and Q. W. Shi, *Surf. Interfaces*, 2025, **59**, 105930.
117 H. Q. Liu, X. R. Chen, D. H. Li, L. X. Liu and L. C. Li, *Surf. Sci.*, 2023, **728**, 122198.
118 Y. Q. Zhong, R. Wang, J. H. Chen, C. Duan, Z. Y. Huang, S. Yu, H. Guo and Y. Zhou, *ACS Appl. Mater. Interfaces*, 2022, **14**(15), 17601–17609.
119 W. Gan, X. C. Fu, J. Guo, M. Zhang, H. Yu, C. S. Ding, S. H. Qi, X. Y. Cao and Z. Q. Sun, *J. Alloys Compd.*, 2022, **909**, 164737.
120 Z. S. Wei, L. M. Wu, X. Yue, H. R. Mu, Z. H. Li, Y. Chang, M. Janczarek, S. Juodkazis and E. Kowalska, *Appl. Catal., B*, 2024, **345**, 123654.
121 P. Innocenzi and L. Malfatti, *J. Photochem. Photobiol., C*, 2024, **58**, 100646.
122 M. V. Diamanti, M. V. Shinnur, M. P. Pedeferri, A. M. Ferrari, R. Rosa and D. Meroni, *Adv. Sustainable Syst.*, 2025, 2401017.
123 A. A. Shmelev, R. V. Shafigulin and A. V. Bulanova, *React. Kinet. Mech. Catal.*, 2022, **135**(2), 1047–1058.
124 L. Q. Zhang, C. Wang, J. Sun and Z. K. An, *Catalysts*, 2020, **10**(5), 575.
125 H. Kim and W. Choi, *Appl. Catal., B*, 2007, **69**(3–4), 127–132.
126 S. M. Wu and P. Schmuki, *Energy Technol.*, 2023, **11**(7), 2300052.
127 R. J. Xie, D. X. Lei, Y. J. Zhan, B. Y. Liu, C. H. A. Tsang, Y. X. Zeng, K. Li, D. Y. C. Leung and H. B. Huang, *Chem. Eng. J.*, 2020, **386**, 121025.
128 B. Yu, L. H. Zhang, H. B. Wu, J. Wen, A. M. Ali, H. Zhang, G. P. Zhang and M. W. Yu, *Chem. Phys. Lett.*, 2022, **801**, 139710.
129 F. Puga, J. A. Navío, C. Jaramillo-Páez, P. Sánchez-Cid and M. C. Hidalgo, *J. Photochem. Photobiol., A*, 2020, **394**, 112457.
130 Q. Q. Wang, S. L. Zhu, Y. Q. Liang, Z. D. Cui, X. J. Yang, C. Y. Liang and A. Inoue, *J. Nanopart. Res.*, 2017, **19**(2), 72.
131 S. Ali, P. M. Ismail, M. Khan, A. Dang, S. Ali, A. Zada, F. Raziq, I. Khan, M. S. Khan, M. Ateeq, W. Khan, S. H. Bakhtiar, H. Ali, X. Q. Wu, M. I. A. Shah, A. Vinu, J. B. Yi, P. F. Xia and L. Qiao, *Nanoscale*, 2024, **16**(9), 4352–4377.
132 J. Wang, C. Q. Yang, D. Q. Ye and Y. Hu, *Appl. Catal., B*, 2025, **361**, 124635.
133 W. W. Yang and Q. W. Bu, *Mater. Lett.*, 2024, **367**, 136619.
134 H. H. Lemago, L. Tolezani, T. Igricz, D. Hessz, P. Pál, C. Cserháti, G. Vecsei, B. Sárközi, E. M. Baradács, Z. Erdélyi and I. M. Szilágyi, *Ceram. Int.*, 2025, **51**(1), 339–352.
135 H. Tada and S. I. Naya, *Catalysts*, 2021, **11**(2), 205.
136 J. H. Yuan, Q. L. Chen, Y. Q. Wang, S. M. Zhou and S. Y. Lou, *Mater. Today Commun.*, 2025, **43**, 111576.
137 J. T. Tang, X. L. Wang, Y. S. Huang, X. P. Du, Z. Q. He, D. Wang and S. Song, *Chem. Eng. J.*, 2024, **499**, 156055.

138 C. Mrabet, R. Jaballah and M. Moussa, *Mater. Sci. Semicond. Process.*, 2024, **184**, 108801.
139 Y. Yang, S. H. Zhao, F. K. Bi, J. F. Chen, Y. X. Wang, L. F. Cui, J. C. Xu and X. D. Zhang, *Appl. Catal., B*, 2022, **315**, 121550.
140 Z. L. Qi, J. C. Li and B. Chen, *J. Phys. Chem. C*, 2020, **124**(46), 25529–25537.
141 Q. Zhou, K. J. Zhang, Y. R. Su, X. H. Wu, T. Y. Gao and G. H. Wang, *J. Materiomics*, 2025, **11**(4), 100987.
142 S. Kim, H. K. Chang, K. B. Kim, H. J. Kim, H. N. Lee, T. J. Park and Y. M. Park, *Catalysts*, 2021, **11**(10), 1144.
143 D. Pradhan, S. K. Biswal, R. Pattanaik, N. Nayak and S. K. Dash, *New J. Chem.*, 2024, **48**(38), 16853–16868.
144 S. L. Lv, K. Wang, T. L. Dang, X. P. Li, K. X. Dai, Z. H. He, H. Wang, W. T. Wang, X. J. Lai and Z. T. Liu, *J. Colloid Interface Sci.*, 2025, **689**, 137214.
145 F. Y. Jian, N. Lu, S. J. Zhao, H. T. Liang, Z. H. Wei, A. Liu and H. Tang, *J. Alloys Compd.*, 2025, **1014**, 178641.
146 R. M. Ma, G. Williams, M. Muscetta and S. Vernuccio, *Chem. Eng. J.*, 2025, **507**, 160228.
147 C. Y. Zhang, S. Y. Zhang and X. X. Li, *Funct. Mater. Lett.*, 2025, **18**(2), 2551016.
148 X. X. Zhan, C. H. Ding, Q. H. Zhao and Y. X. Fang, *Opt. Mater.*, 2024, **155**, 115860.
149 Q. Q. Huang, Y. Hu, Y. Pei, J. H. Zhang and M. L. Fu, *Appl. Catal., B*, 2019, **259**, 118106.
150 S. J. Phang, V. L. Wong, L. L. Tan and S. P. Chai, *Appl. Mater. Today*, 2020, **20**, 100741.
151 D. R. Eddy, M. D. Permana, L. K. Sakti, G. A. N. Sheha, Solihudin, S. Hidayat, T. Takei, N. Kumada and I. Rahayu, *Nanomaterials*, 2023, **13**(4), 704.
152 A. S. Malik and L. A. Fredin, *Phys. Chem. Chem. Phys.*, 2023, **25**(3), 2203–2211.
153 L. Ren, Y. Z. Li, M. Y. Mao, L. Lan, X. B. Lao and X. J. Zhao, *Appl. Surf. Sci.*, 2019, **490**, 283–292.
154 S. Kashiwaya, T. Toupance, A. Klein and W. Jaegermann, *Adv. Energy Mater.*, 2018, **8**(33), 1802195.
155 L. Roebuck, H. Daly, L. Lan, J. Parker, A. Gostick, N. Skillen, S. J. Haigh, M. Falkowska and C. Hardacre, *J. Catal.*, 2025, **442**, 115876.
156 J. S. Qu, J. D. He, H. Li, Q. K. Jiang, M. R. Li, Q. K. Kong, M. Shi, R. G. Li and C. Li, *J. Phys. Chem. C*, 2023, **127**(1), 768–775.
157 L. L. Zhou, Z. Z. Shen, S. B. Wang, J. X. Gao, L. L. Tang, J. Li, Y. M. Dong, Z. Y. Wang and J. Z. Lyu, *Ceram. Int.*, 2021, **47**(15), 21090–21098.
158 X. X. Wang, Q. Ni, D. W. Zeng, G. L. Liao and C. S. Xie, *Appl. Surf. Sci.*, 2016, **389**, 165–172.
159 J. Z. Lyu, J. X. Gao, M. Zhang, Q. Fu, L. N. Sun, S. Hu, J. B. Zhong, S. Wang and J. Li, *Appl. Catal., B*, 2017, **202**, 664–670.
160 H. A. Maitlo, S. A. Younis, K. H. Kim, W. F. Yue, Z. S. Lu and D. H. Lim, *ACS Appl. Mater. Interfaces*, 2025, **17**(3), 4711–4727.
161 D. J. Kim, J. Park, G. Ham, H. Cha, D. S. Han, M. Kim and H. Park, *ACS ES&T Eng.*, 2024, **4**(10), 2474–2484.
162 K. M. Zhang, J. X. Wang, R. Ninakanti and S. W. Verbruggen, *Chem. Eng. J.*, 2023, **474**, 145188.
163 E. Gezmis-Yavuz, C. E. Cansoy and D. Y. Koseoglu-Imer, *J. Environ. Chem. Eng.*, 2023, **11**(3), 110067.
164 J. Li, J. F. Zheng, X. M. Liu and Z. G. Huang, *Mol. Catal.*, 2023, **544**, 113176.
165 S. Sumitsawan, J. Cho, M. L. Sattler and R. B. Timmons, *Environ. Sci. Technol.*, 2011, **45**, 6970–6977.
166 H. Ichiura, T. Seike and A. Kozu, *Chemosphere*, 2020, **256**, 127143.
167 F. He, W. Jeon and W. Choi, *Nat. Commun.*, 2021, **12**(1), 2528.
168 S. Kundu and N. Karak, *Chem. Eng. J.*, 2022, **438**, 135575.
169 W. J. Liu, W. Q. Li, H. R. Wang, H. Y. Bian and K. Zhang, *Adv. Eng. Mater.*, 2023, **25**(21), 2300765.
170 G. Liu, L. J. Han, J. W. Wang, Y. Q. Yang, Z. Y. Chen, B. L. Liu and X. C. An, *J. Mater. Sci. Technol.*, 2024, **174**, 188–194.
171 D. Wood, S. Shaw, T. Cawte, E. Shanen and B. V. Heyst, *Chem. Eng. J.*, 2020, **391**, 123490.
172 B. Borazjani and A. A. Khakpoor, *Surf. Interfaces*, 2025, **59**, 105914.
173 J. Yu, J. Y. Lei, L. Z. Wang, J. L. Zhang and Y. D. Liu, *J. Alloys Compd.*, 2018, **769**, 740–757.
174 Y. Xu, X. Zhu, Y. Dan, J. H. Moon, V. W. Chen, A. T. Johnson and S. Yang, *Chem. Mater.*, 2008, **20**(5), 1816–1823.
175 M. Lafjah, A. Mayoufi, E. Schaal, F. Djafri, A. Bengueddach, N. Keller and V. Keller, *Catal. Today*, 2014, **235**, 193–200.
176 S. J. Armaković and S. Armaković, *Catalysts*, 2025, **15**(2), 174.
177 S. Boufi, S. Bouattour, A. M. Ferraria, L. F. V. Ferreira, A. M. B. Rego, M. M. Chehimi and M. R. Vilar, *Nanotechnol. Rev.*, 2019, **8**(1), 671–680.
178 B. M. Everhart, B. McAuley, A. A. Mayyahi, B. Tonyali, U. Yucel and P. B. Amama, *Chem. Eng. J.*, 2022, **446**, 136984.
179 Q. Xin, H. D. Zhang, Z. J. Zhan, P. T. Shao and M. Zhang, *Constr. Build. Mater.*, 2025, **472**, 140919.
180 L. Zhong, C. S. Lee and F. Haghighat, *J. Hazard. Mater.*, 2012, **243**, 340–349.
181 T. Ahmed, T. Farooq, K. Ahmed, M. A. U. Rehman, M. Yasir, S. Butt and M. A. Basit, *Colloids Surf., A*, 2024, **691**, 133850.
182 M. Li, B. Lu, Q. F. Ke, Y. J. Guo and Y. P. Guo, *J. Hazard. Mater.*, 2017, **333**, 88–98.